
Research Articles: Systems/Circuits

Single-cell membrane potential fluctuations evince network scale-freeness and quasicriticality

James K Johnson, Nathaniel C. Wright, Ji Xia (夏霁) and Ralf Wessel

Washington University, Department of Physics — Compton Hall, One Brookings Dr. — Campus Box 1105, St. Louis, MO 63130

<https://doi.org/10.1523/JNEUROSCI.3163-18.2019>

Received: 17 December 2018

Revised: 1 March 2019

Accepted: 25 March 2019

Published: 5 April 2019

Author contributions: J.K.J., N.C.W., and R.W. designed research; J.K.J. analyzed data; J.K.J. wrote the first draft of the paper; J.K.J., N.C.W., J.X., and R.W. edited the paper; J.K.J. wrote the paper; N.C.W. performed research; J.X. contributed unpublished reagents/analytic tools.

Conflict of Interest: The authors declare no competing financial interests.

Woodrow Shew at the University of Arkansas for helping with the comparison to MEA data. Nathaniel (Caleb) Wright is now at Georgia Institute of Technology, Dept. of Biomedical Engineering., This research was supported by a Whitehall Foundation grant (no. 20121221; R. Wessel) and a National Science Foundation Collaborative Research in Computational Neuroscience grant (no. 1308159; R. Wessel).

Corresponding: James K Johnson: Designed experiments, analyzed data, drafted manuscript, jkjohnson@wustl.edu, cid.org/0000-0003-4014-3244

Cite as: J. Neurosci 2019; 10.1523/JNEUROSCI.3163-18.2019

Alerts: Sign up at www.jneurosci.org/alerts to receive customized email alerts when the fully formatted version of this article is published.

Title page

Title:

Single-cell membrane potential fluctuations evince network scale-freeness and quasicriticality

Abbreviated title:

Single-cell V_m shows scale-free critical network

Author names, roles, phone, and email:

James K Johnson:

Designed experiments, analyzed data, drafted manuscript (Corresponding, and submitting author)

jkjohnson@wustl.edu

orcid.org/0000-0003-4014-3244

Nathaniel C. Wright:

Designed experiments, performed experiments

nathaniel.wright@bme.gatech.edu

Ji Xia (夏霁):

Software development, manuscript preparation

xiaji@wustl.edu

Ralf Wessel:

Designed experiments, manuscript preparation (Principal investigator)

rw@wustl.edu

Author Affiliations:

All authors:

Washington University

Department of Physics – Compton Hall

One Brookings Dr. – Campus Box 1105

St. Louis, MO 63130

Manuscript formatting details:

67 pages

7 figures

248 word abstract

118 word significance statement

650 word introduction

1500 word discussion

Conflicts of interest:

The authors declare no competing financial interests

Acknowledgements:

Woodrow Shew at the University of Arkansas for helping with the comparison to MEA data. Nathaniel (Caleb)

Wright is now at Georgia Institute of Technology, Dept. of Biomedical Engineering.

This research was supported by a Whitehall Foundation grant (no. 20121221; R. Wessel) and a National Science Foundation Collaborative Research in Computational Neuroscience grant (no. 1308159; R. Wessel).

Journal section:

Systems/Circuits

Key words:

criticality, neural computation, balanced networks, neuronal avalanches, membrane potential, renormalization group

1

Abstract

2

What information single neurons receive about general neural circuit activity is a fundamental question for neuroscience. Somatic membrane potential fluctuations are driven by the convergence of synaptic inputs from a diverse cross-section of upstream neurons. Furthermore, neural activity is often scale-free implying that some measurements should be the same, whether taken at large or small scales. Together, convergence and scale-freeness support the hypothesis that single membrane potential recordings carry useful information about high-dimensional cortical activity. Conveniently, the theory of “critical branching networks” (one purported explanation for scale-freeness) provides testable predictions about scale-free measurements which are readily applied to membrane potential fluctuations. To investigate, we obtained whole-cell current clamp recordings of pyramidal neurons in visual cortex of turtles with unknown genders. We isolated fluctuations in membrane potential below the firing threshold and analyzed them by adapting the definition of “neuronal avalanches” (spurts of population spiking). The membrane potential fluctuations we analyzed were scale-free and consistent with critical branching. These findings recapitulated results from large-scale cortical population data obtained separately in complementary experiments using microelectrode arrays (previously published (Shew et al., 2015)). Simultaneously recorded single-unit local field potential did not provide a good match, demonstrating the specific utility of membrane potential. Modeling shows that estimation of dynamical network properties from neuronal inputs is most accurate when networks are structured as critical branching networks. In conclusion, these findings extend evidence of critical phenomena while also establishing subthreshold pyramidal neuron membrane potential fluctuations as an informative gauge of high-dimensional cortical population activity.

20

21

Significance Statement

22

23

24

25

26

27

28

29

30

31

The relationship between membrane potential dynamics of single neurons and population dynamics is indispensable to understanding cortical circuits. Just as important to the biophysics of computation are emergent properties such as scale-freeness, where critical branching networks offer insight. This report makes progress on both fronts by comparing statistics from single-neuron whole-cell recordings to population statistics obtained with microelectrode arrays. Not only are fluctuations of somatic membrane potential scale-free, they match fluctuations of population activity. Thus, our results demonstrate appropriation of the brain's own subsampling method (convergence of synaptic inputs), while extending the range of fundamental evidence for critical phenomena in neural systems from the previously observed mesoscale (fMRI, LFP, population spiking) to the microscale, namely, membrane potential fluctuations.

32

Introduction

33 How do cortical population dynamics impact single neurons? What can we learn about cortical population
34 dynamics from single neurons? These questions are central to neuroscience. Uncovering the functional significance
35 of multiscale organization within cerebral cortex requires knowing the relationship between the dynamics of
36 networks and individual neurons within them (Nunez et al., 2013).

37 For pyramidal neurons in the visual cortex, somatic spike generation is ambiguously related to presynaptic
38 firing (Tsodyks and Markram, 1997; Brunel et al., 2014; Gatys et al., 2015; Stuart and Spruston, 2015; Moore et al.,
39 2017). Such neurons pass spiking information to many postsynaptic neurons (Lee et al., 2016). However, a
40 presynaptic pool with multifarious neighboring and distant neurons (Hellwig, 2000; Wertz et al., 2015) provides
41 excitatory and inhibitory synaptic inputs throughout the soma and complex dendritic architecture (Magee, 2000;
42 Larkum et al., 2008; Moore et al., 2017). Input propagation to the axon hillock has both active and passive features
43 (London and Häusser, 2005), and the membrane potential (V_m) response is increasingly non-linear near the action
44 potential threshold. Thus, such details of network propagation give membrane potential more utility than focusing
45 solely on spiking.

46 Most computational neuroscientists use spiking data because spikes are “the currency of the brain”
47 (Wolfe et al., 2010), and extracellular recording is straightforward compared to whole-cell recording. Yet, the
48 paucity of single-neuron spiking (Shoham et al., 2006), and limited foreknowledge about connections
49 (Helmstaedter, 2013) makes extracellular single-unit observation an impoverished means of studying neuronal
50 circuits. In contrast, subthreshold V_m fluctuations contain rich information about the circuits containing each
51 neuron (Sachidhanandam et al., 2013; Petersen, 2017). Integral to gaining a neuron’s view of the brain is
52 uncovering relationships between the statistics of V_m fluctuations and fluctuations of local spiking; then
53 contrasting against other plausible one-dimensional signals.

54 We look for such relationships in the strict predictions and rigorous measurements of scale-freeness used
55 to identify a fragile network connectivity pattern known as “critical branching”. This pattern exhibits emergent
56 properties valuable for information processing, such as higher susceptibility and dynamic range (Haldeman and

57 Beggs, 2005; Beggs, 2008; Shew and Plenz, 2012; Shriki and Yellin, 2016; Timme et al., 2016), but omits some
58 neuronal dynamics (Poil et al., 2008, 2012) without extension (Porta and Copelli, 2018). The pattern is as follows:
59 on average over all neuronal avalanches (spiking above baseline (Friedman et al., 2012)), one spike leads to *exactly*
60 one other spike. In most arbitrary networks there is less or more than one; these are “subcritical” and
61 “supercritical” respectively. Among the dazzling emergent properties of “criticality” are universality, self-similarity,
62 and scale-free correlations (Stanley, 1999).

63 These are as follows: A “universality class” is a set of incongruous systems exhibiting identical statistics
64 only at their “critical points”. “Self-similarity” includes fractal patterns and power-laws in geometrical analysis of
65 avalanches (power-laws are “scale-invariant”, popularly called “scale-free”). Avalanches of any duration have
66 identical average shapes after normalization (Shaukat and Thivierge, 2016). Avalanche areas grow with duration as
67 another power-law (Sethna et al., 2001). However, observation methods must be consistent with event
68 propagation (Priesemann et al., 2009; Yu et al., 2014; Levina and Priesemann, 2017). Additionally, pairwise
69 correlation vs length or time are also power-laws (Chialvo, 2010) meaning any input has a nonzero chance of
70 propagating forever or anywhere.

71 In summary, the theory of critical branching networks offers superb standards of comparison for three
72 reasons: neuronal avalanche analysis applies to membrane potentials, offers promising insights, and makes precise
73 predictions about fluctuation geometry. We study both V_m fluctuations and criticality with one simple question: Do
74 V_m fluctuations match the scale-free statistics of cortical populations (**Figure 1**)?

75 To address this question, we simultaneously recorded somatic V_m from pyramidal neurons and local field
76 potential (LFP) in visual cortex and performed avalanche analysis on fluctuations. We found that subthreshold V_m
77 fluctuation statistics match published microelectrode array (MEA) data. We used surrogate testing to show why
78 negative LFP fluctuations don’t match and modeling to demonstrate dependence on critical branching.

79

80

Methods**81 Surgery and Visual Cortex**

82 All procedures were approved by Washington University's Institutional Animal Care and Use Committees
83 and conform to the guidelines of the National Institutes of Health on the Care and Use of Laboratory Animals.
84 Fourteen adult red-eared sliders (*Trachemys scripta elegans*, 150-1000 g) were used for this study, their genders
85 were not recorded. Turtles were anesthetized with Propofol (2 mg Propofol/kg), then decapitated. Dissection
86 proceeded as described previously (Saha et al., 2011; Crockett et al., 2015; Wright et al., 2017a).

87 To summarize, immediately after decapitation, the brain was excised from the skull, with right eye intact,
88 and bathed in cold extracellular saline (in mM, 85 NaCl, 2 KCl, 2 MgCl₂*6H₂O, 20 Dextrose, 3 CaCl₂-2H₂O, 45
89 NaHCO₃). The dura was removed from the left cortex and right optic nerve, and the right eye hemisected to expose
90 the retina. The rostral tip of the olfactory bulb was removed, exposing the ventricle that spans the olfactory bulb
91 and cortex. A cut was made along the midline from the rostral end of the remaining olfactory bulb to the caudal
92 end of the cortex. The preparation was then transferred to a perfusion chamber (Warner RC-27LD recording
93 chamber mounted to PM-7D platform) and placed directly on a glass coverslip surrounded by Sylgard. A final cut
94 was made to the cortex (orthogonal to the previous and stopping short of the border between medial and lateral
95 cortex) allowing the cortex to be pinned flat, with ventricular surface exposed. Multiple perfusion lines delivered
96 extracellular saline to the brain and retina in the recording chamber (adjusted to pH 7.4 at room temperature).

97 We used a phenomenological approach to identify the visual cortex, described previously (Shew et al.,
98 2015). In brief, this region was centered on the anterior lateral cortex, in agreement with voltage-sensitive dye
99 studies (Senseman and Robbins, 1999, 2002). Anatomical studies identify this as a region of cortex receiving
100 projections from lateral geniculate nucleus (Mulligan and Ulinski, 1990). We further identified a region of neurons
101 as belonging to the visual cortex when the average LFP response to visual stimulation crossed a given threshold
102 and patched within that neighborhood (radius of about 300 μ m).

103

104 Intracellular Recordings

105 For whole-cell current clamp recordings, patch pipettes (4-8 M Ω) were pulled from borosilicate glass and filled
106 with a standard electrode solution (in mM; 124 KMeSO₄, 2.3 CaCl₂·2H₂O, 1.2 MgCl₂, 10 HEPES, 5 EGTA) adjusted to
107 pH 7.4 at room temperature. Cells were targeted for patching using a differential interference contrast microscope
108 (Olympus). Membrane potential recordings were collected using an Axoclamp 900A amplifier, digitized by a data
109 acquisition panel (National Instruments PCIe-6321), and recorded using a custom LabVIEW program (National
110 Instruments), sampling at 10 kHz. As described in (Crockett et al., 2015; Wright and Wessel, 2017; Wright et al.,
111 2017b, 2017a), before recording from a cell after initial patching current was injected to elicit spiking. This was also
112 repeated intermittently between recording trials. Recording did not proceed if a cell spiked inconsistently (failure
113 to spike, insufficient spike amplitude) in response to injected current, or exhibited extreme depolarization in
114 response to small current injection amplitudes. If a clog or loss of seal was suggested by unusually erratic
115 membrane potential short timescales current the current injection test was performed and upon failure, the
116 affected recording was marked for exclusion from analysis. We excluded cells that did not display stable resting
117 membrane potentials for long enough to gather enough avalanches. Up to 3 whole-cell recordings were made
118 simultaneously. In total, we obtained recordings from 51 neurons from 14 turtles.

119 Recorded V_m fluctuations taken in the dark (no visual stimulation) were interpreted as ongoing activity.
120 Such ongoing cortical activity was interrupted by visual stimulation of the retina with whole-field flashes and
121 naturalistic movies as described previously (Wright and Wessel, 2017; Wright et al., 2017a, 2017b). An
122 uninterrupted recording of ongoing activity lasted for 2 to 5 minutes. Periods of visual stimulation were too short
123 and were too frequently interrupted by action potentials to yield the great number of avalanches which are
124 required for rigorous power-law fitting.

125 A sine-wave removal algorithm was used to remove 60 Hz line noise. Action potentials in turtle cortical
126 pyramidal neurons are relatively rare. An algorithm was used to detect spikes, the V_m recordings between spikes
127 were extracted and filtered from 0 to 100 Hz. Membrane potential recordings were detrended by subtracting the
128 5th percentile in a sliding 2 s window. The resulting signal was then shifted to have the same mean value as before
129 subtraction. De-trending did not affect the size of membrane potential fluctuations (data not shown).

130

131 **Extracellular Recordings**

132 Extracellular recordings were achieved with tungsten microelectrodes (microprobes heat-treated tapered
133 tip), with approximately 0.5 M Ω impedance. Electrodes were slowly advanced through tissue under visual
134 guidance using a manipulator (Narishige), while monitoring for activity using custom acquisition software (National
135 Instruments). The extracellular recording electrode was located within approximately 300 μ m of patched neurons.
136 Extracellular activity was collected using an A-M Systems Model 1800 amplifier, band-pass filtered between 1 Hz
137 and 20,000 Hz, digitized (NI PCIe-6231), and processed using custom software (National Instruments). Extracellular
138 recordings were down-sampled to 10,000 Hz and then filtered (100 Hz low-pass), yielding the local field potential
139 (LFP). The LFP was filtered and detrended as described above (see Intracellular Recordings), except that the mean
140 of the entire signal was subtracted, and the signal was multiplied by -1 before it was detrended. This final inverted
141 signal is commonly featured in literature as negative LFP or nLFP (Kelly et al., 2010; Kajikawa and Schroeder, 2011;
142 Okun et al., 2015; Ness et al., 2016).

143

144 **Experimental Design and Statistical Analysis**

145 **Set-wise comparisons.**

146 In order to measure differences between sets of statistics we rely on three non-parametric measures. We
147 use the MATLAB Statistics and Machine Learning Toolbox implementation of Fisher's exact test (Hammond et al.,
148 2015). This lets us measure the effect size (Odds Ratio r_{OR}) and statistical significance (p value) of finding that
149 consistency with criticality is more frequent or less frequent in an experimental group than a control group.

150 To quantify the similarity between the exponents measured in different sets of data we use the MATLAB
151 Statistics and Machine Learning Toolbox implementations of the *exact* Wilcoxon rank sum test (Hammond et al.,
152 2015) and the *exact* Wilcoxon signed rank test. In both cases effect size, r_{SDF} is measured by the simple difference
153 formula (Kerby, 2014). The rank sum test is used when comparing non-simultaneous recordings, such as comparing
154 MEA data with V_m data. The signed rank test is used when comparing data that can be paired, such as V_m data to
155 concurrent LFP. When comparing whether a dataset differs from a specific value, we can use the sign test.

156 The significance level is set at $p=0.05$ for all tests. Each set-wise comparison test stands alone as its own
157 conclusion. None are combined to assess the significance of any effect across sets-of-sets. Thus, we are not making
158 multiple comparisons and no corrections are warranted (Bender and Lange, 2001).

159

160 **Random surrogate testing.**

161 It is possible that scale-free observations have an origin in independent random processes of a kind
162 previously demonstrated (Touboul and Destexhe, 2017). To control for this, we phase-shuffled the V_m fluctuations
163 using the amplitude adjusted Fourier transform (AAFT) algorithm (Theiler et al., 1992). This tests against the null
164 hypothesis that a measure on a time series can be reproduced by performing a non-linear rescaling of a linear
165 Gaussian process with the same autocorrelation (same Fourier amplitudes) as the original process. Phase
166 information is randomized, which removes higher-order correlations but preserves the scale-free power-spectrum.

167 The AAFT tests only higher-order correlations, but a simpler algorithm tests against the null hypothesis
168 that an *un-rescaled* linear Gaussian process with the same autocorrelation as the original process can produce the
169 same results (Theiler et al., 1992). This is known as the Unwindowed Fourier Transform (UFT). Once we see what
170 measures depend on the higher-order correlations with the AAFT we can use the UFT to see how measures
171 depend on the non-Gaussianity (non-linear rescaling) which is inherent to excitable membranes. Using the UFT
172 alone would make it difficult to attribute whether statistically significant differences are due to the rescaling or to
173 the higher-order correlations (Rapp et al., 1994).

174 We performed AAFT and UFT on each V_m time series once, and then compared how the two datasets
175 performed on every metric used in this study. The datasets were compared with a matched Wilcoxon sign rank test
176 implemented via MATLAB's statistics tool box. Doing the comparison at a dataset level allowed us to obtain a
177 discrimination statistic for every metric we used without repeating the computationally expensive analysis
178 procedure hundreds or thousands of times on every V_m trace. With enough individual recordings in each dataset
179 the matched Wilcoxon sign rank test is a reliable measure, which empowered us to efficiently compare all

180 important metrics.

181

182 **Neuronal avalanche analysis.**

183 Neuronal avalanches were defined by methods analogous to (Poil et al., 2012), which are used for
184 uninterrupted ongoing signals whereas methods based on event detection (Beggs and Plenz, 2003) require periods
185 of non-activity. A threshold is defined, and an avalanche starts when the signal crosses the threshold from below
186 and ends when the signal crosses the threshold from above. The choice of threshold is a free parameter and we set
187 it to the 25th percentile before conducting the complete analysis. In similar situations (continuous non-zero
188 signals) researchers chose $\frac{1}{2}$ the median (Poil et al., 2012; Larremore et al., 2014). However, $\frac{1}{2}$ the median cannot
189 work for negative signals or signals with high mean but low variance. Before analysis threshold choices between
190 the 15th to 50th percentile were tested on data from the five cells with the most recordings to see how threshold
191 may affect the number of avalanches. The 25th percentile was in keeping with the existing literature and gave
192 many avalanches compared to alternatives. Having a large number of avalanches is important because it gives the
193 best statistical resolution. An analysis with a choice of threshold that yields fewer avalanches (or changing the
194 threshold for each recording) would be suspect for selecting serendipitous results. After the analysis was
195 conducted eight percentiles between the 15th to 50th were tested and gave similar power-law exponents.

196 We quantified each neuronal avalanche by its size A and its duration D . The avalanche size is the area
197 between the processed V_m recording and the baseline. The baseline is another free parameter that was set at the
198 second percentile of the processed V_m recording. The second percentile was chosen because its value is more
199 stable than the absolute minimum. The avalanche duration D is the time between threshold crossings.

200 The lower limit of avalanche duration is defined by the membrane time constant which has been reported
201 to be between 50 and 140 ms for the turtle brain at room temperature (Ulinski, 1990; Larkum et al., 2008). We
202 took a conservative approach by setting the limit at less than half the lower bound on membrane time constant
203 which was significantly less than the lower cut-off from power-law fits. Only avalanches of duration larger than 20

204 ms were included in the analysis. Thus, we avoided artificially retaining only the events most likely to be power-law
205 distributed.

206 Following the procedure described above, each processed V_m recording of uninterrupted ongoing activity
207 (i.e., a recording of 2 to 5 minutes duration) yielded 327 ± 148 (mean \pm standard deviation) avalanches. This is
208 insufficient for rigorous statistical fitting on recordings individually (Clauset et al., 2009). Therefore, we grouped
209 avalanches from multiple recordings of ongoing activity of the same cells. Each cell produced between 3 and 19
210 recordings of ongoing activity (2 to 5 minutes duration each recording), with trials recorded intermittently over a
211 period of 10 to 60 minutes. We grouped recordings based on whether they occurred in the first or second 20-
212 minute period since the beginning of recording from that neuron. Then all the avalanches from the first or second
213 20-minute period were grouped together with one data object (the group) storing the size, and duration of each
214 avalanche. It is rare for neurons to have recordings in the third 20-minute periods, so this data was not included.
215 Since there was a slow drift in the mean membrane potential over a period of several minutes, we scaled the
216 avalanche sizes from each recording to have the same median as other recordings from the same group. Z-scoring
217 was not useful for accounting for trial to trial variability because it does affect whether a specific time-point is
218 above or below a certain percentile threshold. Therefore, it is not useful for removing variability in avalanche
219 duration. Windowed z-scoring introduces artifacts near action potentials. On average 4 recordings were possible in
220 each 20-minute period. There were 51 neurons with multiple recordings of ongoing activity in the first 20-minutes
221 of experimentation (thus 51 recording groups). Of these, 18 neurons had an additional 20-minute period with
222 more than one recording. This produced a total of 69 groups with 1346 ± 1018 (mean \pm standard deviation)
223 avalanches for each group. Of these 69 groups, 57% had more than 1000 avalanches. The largest number of
224 avalanches was 7495 and the smallest was 313. Only 5 groups had less than 500 avalanches. We report on the 51
225 groups from the first 20-minute period separately from the 18 groups with recordings from the second 20-minute
226 period of experimentation.

227 For each group, we evaluated the avalanche size and duration distributions with respect to power laws.
228 To test whether a distribution followed a power law, we applied the rigorous statistical fitting routine described
229 previously (Clauset et al., 2009). We tested three power-law forms: $P(x) \propto x^{-\alpha}$ (with and without truncation)

230 (Deluca and Corral, 2013), as well as a power-law with exponential cut-off $P(x) \propto x^{-\alpha} e^{-x/r}$. We compared these
 231 against lognormal and exponential alternative (non-power-law) hypotheses. Distribution parameters were
 232 estimated using Maximum Likelihood Estimation (MLE) and the best model out of those fitted to the data was
 233 chosen using the Akaike Information Criterion (Bozdogan, 1987). It should be acknowledged that a small power-
 234 law region in the truncated form would be suspect for false positives, likewise for a strong exponential cut-off
 235 (Deluca and Corral, 2013). Finally, to decide whether a fitted model was plausible, pseudo-random datasets were
 236 drawn from a distribution with the estimated parameters and then the fraction which had a lower fit quality
 237 (Kolmogorov-Smirnov distance) than the experimental data was calculated. If this fraction, called the comparison
 238 quotient q , was greater than 0.10, the best fit model (according to the Akaike Information Criterion) was accepted
 239 as the best candidate. Otherwise, the next best model was considered.

240 We applied several additional steps and strict criteria to control for false positives. One such step was
 241 assessing whether the scaling relation was obeyed over the whole avalanche distribution for each group (not just
 242 the portion above the apparent onset of power-law behavior). The scaling relation is another power-law
 243 $\langle A \rangle(D) \propto D^\gamma$ predicting how the measured size of avalanches increase geometrically with increasing duration (on
 244 average). For any data set which has three power-laws, $\langle A \rangle(D) \propto D^\gamma$ (scaling relation), $P(A) \propto A^{-\tau}$ (size
 245 distribution), and $P(D) \propto D^{-\beta}$ (duration distribution), the scaling relation exponent is predicted by the other two
 246 exponents by $\gamma \approx \gamma_p = \frac{(\beta-1)}{(\tau-1)}$ (Scarpetta et al., 2018). Note that $\gamma_p = 1$ is a trivial value because it implies
 247 $\langle A \rangle(D) \propto D$ and that would suggest individual avalanches were just noise symmetric about a constant value. This
 248 would mean that the average avalanche shape is just a flat line at some constant of proportionality, $\mathcal{F}\left(\frac{t-t_0}{D}\right) = a$,
 249 where $\mathcal{F}\left(\frac{t-t_0}{D}\right)$ is a function describing the shape of an avalanche of duration D and t_0 is the beginning of the
 250 avalanche and a is a constant.

251

252 ***Standards for consistency with critical point behavior.***

253 We applied four standardized criteria to provide a transparent and systematic way to produce a binary
254 classification, either "no inconsistencies with activity near a critical point were detected" or "some inconsistencies
255 with activity near a critical point were detected".

256 First, a collection of avalanches must be power-law distributed in both its size and duration distributions.

257 Second, the collection of avalanches must have a power-law scaling relation as determined by $R^2 > 0.95$
258 (coefficient of determination) for linear least squares regression to a log-log plot of average size vs durations:
259 $\log(\langle A \rangle(D)) \sim \gamma \log(D) + b$. This R^2 represents the best that any linear fit can achieve and must include all the
260 avalanches, not a subset. We denote the scaling exponent (slope from linear regression) from this fit as γ_f .

261 Third, the scaling relation exponent predicted by theory (denoted as γ_p) must correspond to a trendline
262 on a log-log scatter plot of $\langle A \rangle(D)$ whose R^2 is within 90% of the best-case fitted trendline from the second
263 criterion. Again, the R^2 for the predicted scaling relation is calculated across all avalanches, and not just the subset
264 above the inferred lower cut-off of power-law behavior (which was found for the first criterion). This cross-
265 validates agreement with theory.

266 Fourth, the fitted scaling relation exponent must be significantly greater than 1: $(\gamma_f - 1) > \sigma_{\gamma_f}$ where
267 σ_{γ_f} is the standard error. This last requirement eliminates scaling that might be trivial in origin. It is measured after
268 getting the fitted scaling relation exponent for all the data so that a dataset standard deviation can be determined.
269 It is necessary to also check that the set of scaling relation exponents from the power-law fits to all avalanche sets
270 is significantly different from 1 at a dataset level. A scaling relation exponent equal to one suggests a linear
271 relationship between mean-size and duration which is not consistent with criticality in neural systems (Haldeman
272 and Beggs, 2005).

273 Our four-criterion test cannot measure distance from a critical point nor eliminate all risk of false
274 positives. To complete our analysis, we also look at three additional factors, whether exponent values match
275 exponent values from *other* experiments as expected from the universality prediction of theory, whether all the
276 exponents within our data set have similar scaling relation predictions, and lastly whether the avalanches within
277 our data set exhibit shape collapse across all the recordings.

278

279 ***Applying shape collapse, quantitative and qualitative analysis.***

280 Shape collapse is a very literal manifestation of scale-invariance (also called “self-similarity”)(Sethna et al.,
 281 2001; Beggs and Plenz, 2003; Friedman et al., 2012; Pruessner, 2012; Timme et al., 2016). Avalanches of different
 282 durations should rise and fall in the same way on average. This average avalanche profile is called a scaling
 283 function. The average avalanche profile for avalanches of duration D is predicted to be $\mathcal{A}(t, D) = D^{(\gamma-1)}\mathcal{F}\left(\frac{t-t_0}{D}\right)$
 284 where $D^{(\gamma-1)}$ is the power-law scaling coefficient which modulates the height of the profile and $\mathcal{F}\left(\frac{t-t_0}{D}\right)$ is the
 285 universal scaling function itself (normalized in time). Shape collapse analysis provides an independent estimate of
 286 the scaling relation exponent γ_{SC} , which is only expected to be accurate at criticality (Sethna et al., 2001; Scarpetta
 287 and Candia, 2013; Shaukat and Thivierge, 2016), and a visual test of conformation to an empirical scaling function.

288 Exponent estimation is very sensitive to the unrelated, intermediate rescaling steps involved in combining
 289 the avalanches from multiple recordings into one group. To get an estimate of the scaling relation exponent for
 290 each group, γ_{SC} , we average the scaling exponents γ_i found individually for each recording in that group (i denotes
 291 the i^{th} recording, SC for “shape collapse”).

292 Naturally, individual avalanche profiles are vectors of variable length D . We must first “rescale in time” to
 293 make them vectors of equal length without losing track of what each vector’s original duration was. We do that by
 294 linearly interpolation with 20 evenly spaced points. So, the j^{th} avalanche profile of the i^{th} recording is denoted as a
 295 20-element vector $\overrightarrow{\Gamma}_{ij}$ (where the top arrow denotes a vector).

296 Next, the set of all profiles from recording i with the *exact same duration* D , denoted as $\mathbf{\Gamma}_{D_i}$ where bold
 297 indicates a set, were averaged and divided by a test scaling factor $D^{(\gamma'_i-1)}$. We define this as $\overrightarrow{\Gamma}_{D_i}(\gamma') =$
 298 $\overrightarrow{\langle \mathbf{\Gamma}_{D_i} \rangle} D^{-(\gamma'_i-1)}$. The prime indicates a test rescaling. The average is over all vectors in the set $\mathbf{\Gamma}_{D_i}$. The choice of γ_i
 299 was optimized using MATLAB’s `fminsearch` function to minimize the mean relative error between the average over
 300 all durations $\overrightarrow{\langle \mathbf{\Gamma}_{D_i} \rangle}(\gamma')$ and the set members $\overrightarrow{\Gamma}_{D_i}(\gamma')$ so that for recording i :

301
$$\gamma_i = \operatorname{argmin}_{\gamma' \in [1,2]} \left\langle \frac{|\overline{\Gamma_{D_i}}(\gamma') - \overline{\Gamma_{D_i}}(\gamma'_i)|}{\langle \Gamma_{D_i}(\gamma') \rangle} \right\rangle.$$

302 This error minimization and applying the rescaling is the “collapse” in “shape-collapse”.

303 Once we have the γ_i for the avalanches in each individual recording of ongoing activity we compare the
 304 average, $\gamma_{SC} = \langle \gamma_i \rangle$, to the predicted and fitted scaling relation exponents for the group of recordings, γ_p and γ_f
 305 (statistical comparison tests are described in a previous section). Thus, quantitative analysis of shape collapse was
 306 done by comparing γ_{SC} , γ_p , and γ_f for each of the 69 groups individually.

307 Visual assessment of how well avalanche profiles can be described by one universal scaling function,
 308 $\mathcal{F}\left(\frac{t-t_0}{D}\right)$ supports the quantitative exponent estimation. This was carried out by averaging all the profiles within
 309 specific *duration bins* (regardless of trial or group) and plotting them on top of one another. A very large number of
 310 avalanches are needed so we combine avalanches from all 69 groups. However, the resting membrane potential
 311 differs from recording to recording and cell to cell. Therefore, avalanche profiles from different recordings are
 312 vertically misaligned. To combine avalanche profiles from different recordings we divided all the profiles by a
 313 scalar value unique to each recording: the time average over all the collapsed profiles. This produce rescaled and
 314 mean-shifted profiles (double prime) $\overline{\Gamma''_{ij}} = \overline{\Gamma'_{ij}} / \langle \Gamma'_{ijk} \rangle$ (where $k \in [1,20]$ denotes the interpolated time point).
 315 The set of avalanches from each recording were thus aligned, but individual variability was preserved and thus
 316 profiles from different recordings could be averaged without introducing artifacts. This set, Γ''_{ij} contained a total
 317 of 106,220 shifted and rescaled profiles for the V_m data.

318 The set of shifted and rescaled profiles falling into a duration bin is denoted Γ''_D . Each duration bin then
 319 provides its own estimate of the scaling function $\langle \overline{\Gamma''_D} \rangle \sim \mathcal{F}\left(\frac{t-t_0}{D}\right)$. For each bin, D was defined as the average
 320 duration of all constituent profiles. If less than 700 avalanches had a particular duration, we included the next
 321 longest duration iteratively until we met or exceeded 700 avalanches. This only applied to long durations. The
 322 choice of 700 was made because it allowed us smooth averaging and without excessively wide duration bin widths.

323 We also assessed the mean curvature of avalanche profiles from the rescaled profile for a particular
 324 duration $\langle \Gamma_D'' \rangle$. This allows us to plot how curvature depends on duration. Mean curvature $\langle \kappa \rangle$ is defined like so (k
 325 still denotes time points):

$$\langle \kappa \rangle(D) = \left\langle \frac{\ddot{F} \left(\frac{t-t_0}{D} \right)}{\left(1 + \dot{F} \left(\frac{t-t_0}{D} \right) \right)^{\frac{3}{2}}} \right\rangle$$

$$\sim \left\langle \frac{\langle \Gamma_D'' \rangle_{(k+1)} - 2\langle \Gamma_D'' \rangle_k + \langle \Gamma_D'' \rangle_{(k-1)}}{\left(1 + \langle \Gamma_D'' \rangle_{(k+1)} - \langle \Gamma_D'' \rangle_k \right)^{\frac{3}{2}}} \right\rangle$$

326 **Model Simulations**

327 We simulated a model network consisting of $N = 10^4$ binary probabilistic model neurons. The model
 328 neurons form a directed random network (Erdős–Rényi random graph), where the probability that neuron j
 329 connects to neuron i is c . In a network of N neurons, this results in a mean in-degree and out-degree of cN . We
 330 tested nine not quite evenly distributed values of connection probabilities $c \in [0.5, 1, 3, 5, 7.5, 10, 15, 20, 25] \times 10^{-2}$.
 331 As discussed in (Kinouchi and Copelli, 2006; Larremore et al., 2011a, 2014) the impact of connectivity on network
 332 dynamics is non-linear, so we take a finer look at smaller connection probabilities, while maintaining thorough
 333 coverage of intermediate connection probabilities.

334 The strength of the connection from neuron j to neuron i is quantified in terms of the network adjacency
 335 or weight matrix W with the fortune of having a simple and intuitive meaning. For each existing connection from
 336 neuron j to neuron i , W_{ij} is the direct change in the probability that neuron i will fire at the next timestep if
 337 neuron j spikes in the current time step.

338 The dynamics of this network is well-characterized by the largest eigenvalue λ of the network weight
 339 matrix W , with criticality occurring at $\lambda = 1$ (Kinouchi and Copelli, 2006; Larremore et al., 2011a, 2011b, 2012,
 340 2014). The physical interpretation of λ is a “branching parameter” (Haldeman and Beggs, 2005) that governs
 341 expected number of spikes immediately caused by the firing of one neuron. If $\lambda = 1$ then one spike causes one
 342 other spike on average, while if $\lambda > 1$ one spike causes more than one on average and vice versa.

343 We tested five different values of largest eigenvalue at, near and far from criticality
 344 $\lambda \in [0.9, 0.95, 1, 1.015, 1.03]$. A fraction χ of the neurons are designated as inhibitory. This is done by multiplying all
 345 outgoing connections of an inhibitory neuron by -1. We tested nine different values of the fraction of inhibitory
 346 neurons in the range from 0 to 0.25, thus including the value 0.2, corresponding to the fraction of inhibitory
 347 neurons in the mammalian cortex (Meinecke and Peters, 1987). The magnitudes of non-zero weights are
 348 independently drawn from a distribution of positive numbers with mean η , where the distribution is uniform on
 349 $[0, 2\eta]$, and η is given by $\eta = \lambda / (cN(1 - 2\chi))$. The maximum eigenvalue is then fine-tuned by dividing W by the
 350 current maximum eigenvalue and set to the exactly desired value $W = \lambda W' / \lambda'$ where W' and λ' are the matrices
 351 and eigenvalues before correction.

352 The binary state $S_i(t)$ of neuron i at time t denotes whether the model neuron spikes ($S_i(t) = 1$) or does
 353 not spike ($S_i(t) = 0$) at time t . At each time step, the states of all neurons are updated synchronously according to
 354 the following update rule:

$$S_i(t) = \theta \left(\sum_j^N W_{ij} S_j(t-1) - \xi_i(t) \right)$$

355 Where $\xi_i(t)$ is a random number on $[0, 1]$ drawn from a uniform distribution, and θ is the Heaviside step
 356 function. In addition to this update rule, a refractory period of one time-step (translated to approximately 2 ms)
 357 was imposed for certain parameter conditions. A simulation begins with initiating the activity of one randomly-
 358 chosen excitatory neuron and continuing the simulation until overall network activity had ceased. The process was
 359 then repeated.

360 From the simulated binary states of 10^4 model neurons, we extracted three measures of simulated
 361 activity. First, the network activity $F(t) = \sum_{i=1}^N S_i(t) / N$ is the fraction of neurons spiking at time t . Second, the
 362 input to model neuron i at time t is $P_i(t) = \sum_j^N W_{ij} S_j(t-1)$, which is almost always positive for our parameters.
 363 Note that $P'_i(t) = P_i(t) \times \Theta(P_i(t))$ directly represents the probability for the neuron to spike at time t . Third, we
 364 constructed a proxy for the V_m signal, $\Phi_i(t) = (\alpha_h * P_i)(t)$, by convolving the input $P_i(t)$ with an alpha function:
 365 $\alpha_h(t) = \frac{t}{h_m} \exp(1 - \frac{t}{h_m})$ with $h_m = 2$ time steps (assumed to be about 4 ms).

366 A total of 405 different parameter combinations (connection density, inhibition, maximum eigenvalue)
367 were simulated. Each combination was simulated 10 times. Based on the connection probability c and the fraction
368 of inhibition χ , we distinguish four regions in parameter space classified according to the behavior of the critical
369 model, i.e., $\lambda = 1$.

370 The first region is the “positive weights” region. Without inhibition activity increases or dies out in
371 accordance with the branching parameter. This region is defined by $\chi = 0$. With moderate inhibition and dense
372 connectivity there is a region of parameter space we call “quiet”; activity lasts only slightly longer than in a system
373 with no inhibition. This region is defined by the ex-post-facto boundaries $c \geq e^{11\chi}/25$ and $\chi > 0$. Further
374 increasing inhibition relative to connection density produces a behavior like “up and down” states (or “telegraph
375 noise”) (Sachdev et al., 2004; Millman et al., 2010). We call this the “switching” regime because network activity
376 switches between a low mean and a high mean. This region is defined by $c < e^{11\chi}/25$, and $c \geq (10e^{12\chi} -$
377 $13)/100$ and $\chi > 0$. When inhibition is high relative to connection density the system enters the “ceaseless”
378 region where stimulating one neuron causes activity that effectively never dies out. An especially attractive feature
379 of this model is that the “ceaseless” and “switching” regimes exhibit sustained self-generated activity. This
380 provides a way to model spontaneous neural activity without externally imposed firing patterns.

381 Refractoriness was studied in the network without inhibition and it was found that dynamic range was
382 inversely proportional to refractory period (Larremore et al., 2011a) but the branching parameter (criticality)
383 displayed no dependence on refractory period (Kinouchi and Copelli, 2006). In the literature which featured
384 inhibition and introduced ceaselessness no refractory was used (Larremore et al., 2014). However, we found that
385 for some networks in the switching regime the maximum eigenvalue was a better predictor of the empirical
386 branching ratio if the refractory period was one timestep. Because this relationship is central to our understanding
387 of criticality in this model, we ran an initial testing cycle before each simulation begins to decide whether to set the
388 refractory period to one timestep or zero. Doing so ensures the network displays critical-like phenomena in all
389 regimes (the maximum eigenvalue of connectivity) but also ensures the model adheres to the practices of the
390 literature.

391 We performed avalanche analysis on each of the simulated signals using the methods described above for
392 membrane potential recordings. If the network is in the switching regime, we only perform analysis on the periods
393 when the network is in the mode (high or low mean) in which it spends the majority of its time. As before, the 25th
394 percentile defined the avalanche threshold. If the signal had negative values, as in the case of single neuron Vm
395 proxies in networks with inhibition, the signal was shifted by subtracting the 2nd percentile. To obtain good
396 statistics, we continued stimulating and extracting avalanches until a simulation either reached 10^4 avalanches, or
397 5×10^3 avalanches and a very large file size or a very long computational time. This ensured there were between
398 two and ten thousand avalanches per trial.

399 **Data and Software Accessibility**

400 All raw data is available at https://github.com/jojker/continuous_signal_avalanche_analysis and the code
401 developed for this analysis is available upon request to the corresponding author: James Kenneth Johnson.

402

403

Results

404 Single-neuron membrane potential (V_m) fluctuations are thought to be dominated by synaptic inputs from
405 multitudes of presynaptic neurons (Stepanyants et al., 2002; Brunel et al., 2014; Petersen, 2017). Since the way
406 neurons integrate their diverse inputs is central to information processing in the brain, it is important that
407 neuroscience gain a thorough understanding of the relationship between subthreshold V_m fluctuations and
408 population activity. A basic step is to compare statistical analyses, especially analyses where a meaningful
409 relationship is expected. We asked whether an avalanche analysis on V_m fluctuations would reveal the same
410 signatures of scale-freeness and critical network dynamics found in measures of population activity (**Figure 1**)
411 (Friedman et al., 2012; Shew et al., 2015; Marshall et al., 2016). To address this comparison across organizational
412 levels, we recorded V_m fluctuations from 51 pyramidal neurons in visual cortex of 14 turtles and assessed evidence
413 for critical network dynamics from these recordings.

414 In a model investigation we corroborated results evaluated the conditions needed to enable inferring
415 dynamical network properties from the inputs to single neurons. Finally, we extended the analysis to other
416 commonly recorded time series of neural activity for comparison with the information content of V_m fluctuations
417 about the dynamical network properties.

418

419 Membrane Potential Fluctuations Reveal Signatures of Critical Point Dynamics

420 We obtained whole-cell recordings from pyramidal neurons in the visual cortex of the turtle ex-vivo eye-
421 attached whole-brain preparation (**Figure 2A**). Recorded V_m fluctuations taken in the dark (no visual stimulation)
422 were interpreted as ongoing activity. We analyzed the recorded ongoing V_m fluctuations employing the concept of
423 “neuronal avalanches” (Beggs and Plenz, 2003; Poil et al., 2012; Shew et al., 2015), which are positive fluctuations
424 of network activity. For continuous time-series such as the V_m recording, one selects a threshold and a baseline.
425 We defined a neuronal avalanche based on the positive threshold crossing followed by a negative threshold
426 crossing of the V_m time series (Poil et al., 2012; Hartley et al., 2014; Larremore et al., 2014; Karimipناه et al.,

427 2017a). We quantified each neuronal avalanche by (i) its size A , i.e., the area between the curve and the baseline,
428 and (ii) its duration D , i.e., the time between threshold crossings (**Figure 2B**).

429 To quantify the statistics of avalanche properties, we applied concepts and notations from the field of
430 “critical phenomena” in statistical physics (Nishimori and Ortiz, 2011; Pruessner, 2012). Because the critical point is
431 such a small target for any naturally occurring self-organization (Pruessner, 2012; Hesse and Gross, 2014; Cocchi et
432 al., 2017) and there is considerable risk of false positives (Taylor et al., 2013; Hartley et al., 2014; Touboul and
433 Destexhe, 2017; Priesemann and Shriki, 2018), asserting criticality in a *new* system or with a *new* tool requires
434 extraordinary evidence. Since this is a new tool, we created four criteria and set quantifiable standards for
435 concluding a system is consistent with criticality based on avalanche power-laws and we completed this exhaustive
436 battery of tests with shape collapse, a geometrical analysis of self-similarity in the avalanche profiles (see Methods:
437 Experimental Design and Statistical Analysis).

438 In brief, we found that both the size and duration distributions of the fluctuations treated as avalanches
439 were consistent with power laws (**Figure 2C**), $P(A) \propto A^{-\tau}$ and $P(D) \propto D^{-\beta}$ matching widely reported exponents
440 (Beggs and Plenz, 2003; Priesemann et al., 2009; Hahn et al., 2010; Klaus et al., 2011; Friedman et al., 2012; Shriki
441 et al., 2013; Priesemann, 2014; Arviv et al., 2015; Shew et al., 2015; Karimipannah et al., 2017b, 2017a), obeyed the
442 scaling relation (**Figure 2D**), and exhibited shape collapse over an expansive set of durations, (**Figure 2E**).

443 Specifically, of the 51 recording groups featuring data from the first 20-minute period of recording from
444 one cell, 98% had power laws in both size and duration distributions. The exponent values for the size distribution
445 were $\tau = 1.91 \pm 0.38$ (median \pm standard deviation). Exponent values for the duration distribution were
446 $\beta = 2.06 \pm 0.48$. Of the 51 neurons with a recording group from the first 20-minutes, 18 had an additional 20-
447 minute period spanning multiple recordings. All of these 18 groups had power-laws in both size and duration, the
448 exponent values for the size distribution were $\tau = 1.87 \pm 0.29$ and the exponent values for the duration
449 distribution were $\beta = 2.21 \pm 0.39$.

450 It is also important to confirm that power-law behavior extends across several orders of magnitude of
451 avalanche durations. We typically demonstrate a power-law distribution over 2.45 ± 0.39 orders of magnitude of

452 duration. For the scaling relation we find a larger span with 2.62 ± 0.23 orders of magnitude across our whole
453 avalanche duration range.

454 Another statistic crucial to signatures of criticality measures the relationship *between* the power-laws
455 describing size and duration of avalanches (Sethna et al., 2001; Beggs and Timme, 2012; Friedman et al., 2012). If
456 the average avalanche size also scales with duration according to $\langle A \rangle(D) \propto D^\gamma$, then the exponent γ is not
457 independent, but rather depends on the exponents τ and β according to $\gamma = (\beta - 1)/(\tau - 1)$ irrespective of
458 criticality (Scarpetta et al., 2018). For critical systems this condition is enforced because avalanche profiles follows
459 the same shape for all durations which means that this prediction is believed to be more precise than for non-
460 critical systems and the exact values are important (Sethna et al., 2001; Nishimori and Ortiz, 2011). We found that
461 average avalanche size scaled with duration $\langle A \rangle(D) \sim D^\gamma$ according to a power law and that the observed values of
462 τ and β provided a good prediction $\gamma = (\beta - 1)/(\tau - 1)$ of the fitted γ (Figure 2D).

463 Specifically, of the 51 recording groups from the first 20-minute period, the fitted scaling relation
464 exponents were $\gamma_f = 1.19 \pm 0.05$, and the predicted scaling relation exponents were $\gamma_p = 1.17 \pm 0.35$. For the
465 additional second 20-minute period (18 groups/neurons), the fitted scaling relation exponents were $\gamma_f = 1.21 \pm$
466 0.05 , and the predicted scaling relation exponents were $\gamma_p = 1.28 \pm 0.21$.

467 To affect a more convincing analysis, we defined four stringent criteria that must be independently
468 satisfied before any set of avalanches can be deemed consistent with network dynamics near a critical point (see
469 Methods: Experimental Design and Statistical Analysis). Overall, of the 69 groups of recordings (which includes 18
470 out of 51 cells twice), 98.6% had power-laws in both the size and duration distributions of avalanches and 92.8%
471 had scaling relations which were well fit by power-laws ($R^2 > 0.95$). All were deemed non-trivial by the test
472 $(\gamma_f - 1) > \sigma_{\gamma_f}$ where σ_{γ_f} is the dataset standard error; $\sigma_{\gamma_f} = 0.051$. The smallest value was $\gamma_f = 1.094$. The
473 fourth constraint, that the R^2 of the predicted scaling relation was within 10% of the best fit scaling relation, was
474 satisfied 85.6% of the time. Together, this set of criteria cannot measure distance from a critical point nor
475 eliminate false positives. However, the take away is that 81% of all recording groups examined were judged to be
476 consistent with network activity near a critical point.

477 Separating out results: 76% of the 51 recording groups from the first 20-minute period, and 94% of the
478 recording groups from the second 20-minute period were judged consistent with criticality. The general pattern is
479 that the first 20-minute period and the second are both consistent with criticality, but the second group meets our
480 criteria much more frequently. This could be an effect related to the length of time we are able to maintain a
481 patch, or it could be that a better patching results in both longer stable recording ability and better inference of
482 dynamical network properties.

483 To further discount the possibility of false positives we investigated whether the avalanches within our
484 data set exhibited “shape collapse” (**Figure 2E**). The scaling relation is a consequence of self-similarity (Sethna et
485 al., 2001; Papanikolaou et al., 2011; Friedman et al., 2012; Marshall et al., 2016; Shaukat and Thivierge, 2016;
486 Cocchi et al., 2017). In other words, avalanches all have the same “hump shape” no matter how long they last, this
487 shape is called the scaling-function or avalanche profile. The shape collapse also provides an independent estimate
488 of the scaling relation exponent γ , if the estimated exponent, γ_{SC} , matches the fitted exponent, γ_f , it is considered
489 strong evidence of critical point behavior. For critical systems, the average avalanche profile of an avalanche of
490 duration D is given as $\mathcal{A}(t, D) = D^{(\gamma-1)}\mathcal{F}\left(\frac{t-t_0}{D}\right)$. Where $D^{(\gamma-1)}$ is a coefficient governing the scaling of height with
491 duration, and $\mathcal{F}\left(\frac{t-t_0}{D}\right)$ is the scaling-function which describes the universal shape of an avalanche at any duration.
492 The similarity of avalanche profiles of different durations is qualitatively judged (Sethna et al., 2001; Beggs and
493 Plenz, 2003; Friedman et al., 2012; Pruessner, 2012; Timme et al., 2016) by plotting empirically estimated scaling
494 functions for several durations on top of one another after they have been rescaled as part of the process of
495 estimating γ_{SC} .

496 We obtained shape collapse across more than one order of magnitude (between about 50 ms to 700 ms)
497 of avalanche durations. Below 50 ms distinct peaks arose. Above 700 ms the profile height grew faster than the
498 power-law scaling that worked for shorter duration avalanches, this is observed as an apparent outlier in **Figure 2E**.
499 This likely marks point where avalanches become so long and so large that they begin to weakly activate the non-
500 linear action potential mechanism of the neuron. When comparing to plausible alternatives to V_m in later sections,
501 we included analysis of mean curvature and avalanche profile peak height along with visual inspection of shape

502 collapse quality (**Figure 2E**). The shape collapse plots begin with short avalanches (20 ms) that are below the
503 median lower cut-off for power-law behavior (which was 256 ms) but are well predicted by the scaling relation.

504 The exponents estimated from the shape collapse were a good match for both the predicted and fitted
505 scaling relation exponents. The groups of recordings from the first 20 minutes yielded $\gamma_{SC} = 1.1868 \pm 0.042$. The
506 average matched absolute percent error was 1.3% with respect to γ_f . A matched signed rank difference of median
507 test revealed that γ_f was not significantly different from γ_{SC} , simple difference effect size $r_{SDF} = 0.089$, p-value
508 $p = 0.063$ ($p < 0.05$ indicates that they are different).

509 This stage of the analysis showed that, when fluctuations of V_m are treated like neuronal avalanches, they
510 are consistent with criticality by the standards of power-laws governing size and duration. We also showed that V_m
511 avalanches exhibit geometrical self-similarity across more than one order of magnitude. These factors showed that
512 the cortical circuits driving fluctuations of membrane potential are consistent with activity near a critical point
513 according to standards of self-similarity. In our next investigation we compared to population data from
514 microelectrode arrays and other results from literature to test whether V_m fluctuations are consistent with the
515 universality requirement of behavior near critical points, and whether they can be used to measure dynamical
516 network properties.

517

518 **Membrane Potential Fluctuations are Consistent with Avalanches from Previously Obtained Microelectrode** 519 **Array LFP Recordings**

520 Importantly, we sought to interpret our results from the analysis of single-neuron V_m fluctuations in the
521 context of the more commonly used analysis of multi-unit spiking activity (Friedman et al., 2012; Shew et al., 2015;
522 Marshall et al., 2016; Karimipناه et al., 2017a) or multi-site local field potential (LFP) event detection from
523 microelectrode array (MEA) data (also known as “multielectrode array”) (Beggs and Plenz, 2003; Shew et al.,
524 2015).

525 In a previous study, avalanche analysis was performed on LFP multi-site MEA recordings from the visual
526 cortex of a different set of 13 ex-vivo eye-attached whole-brain preparations in turtle (Shew et al., 2015).

527 Avalanches were inferred from the steady state (after on response transients but before off response transients) of
528 responses to visual presentation of naturalistic movies as opposed to the resting state activity between
529 presentations (which is where the V_m data come from). Avalanche size and duration distributions followed power
530 laws.

531 The median exponents were $\tau = 1.94 \pm 0.27$ for the avalanche size distributions and $\beta = 2.14 \pm 0.32$ for
532 the avalanche duration distributions (**Figure 3A**). A scaling relation existed with average exponent $\gamma_f = 1.20 \pm$
533 0.06 fitted to the data and $\gamma_p = 1.19 \pm 0.07$ from the average of the predicted scaling based on theory. The
534 scaling power-law extended over 1-2 orders of magnitude. Critical branching was more firmly established in Shew
535 et al., 2015 by analyzing the branching ratio. The branching ratio is the average ratio of events (i.e. spikes) from
536 one moment in time to the next, but only during identified avalanches. A critical branching network has a
537 branching ratio of one, but empirically estimating it requires discrete events and an assiduous choice of time-
538 binning for analysis. Shew et al. found that a branching ratio near one that was robust to reasonable choices of
539 time bin and varied with choice of time-bin in expectation with critical branching. We are not aware of methods
540 for estimating a branching ratio in continuous signals like membrane potential.

541 The set of avalanche size, duration, and scaling relation exponents obtained from membrane potential
542 fluctuations (**Figure 3B**) were not distinguishable from the MEA obtained set. The fitted scaling relation exponent
543 γ_f had the least variability of all three kinds of exponents so it is the most likely to show a difference. Thus, if a
544 difference is not significant it suggests universality more strongly than for the avalanche size τ or duration β
545 distribution exponents.

546 When we limited our analysis to the first twenty-minute period which contained multiple recordings (51
547 cells), neither the fitted scaling relation exponent, nor the predicted scaling relation exponent were significantly
548 different from the MEA results. The Wilcoxon rank-sum difference of medians test against the MEA data yielded
549 ($r_{SDF} = 0.164$, $p = 0.37$), and ($r_{SDF} = 0.08$, $p = 0.67$) respectively. The median exponent values for the size and
550 duration distributions were not significantly different from the median of the MEA data ($r_{SDF} = 0.164$, $p = 0.37$)
551 and ($r_{SDF} = 204$, $p = 0.265$) respectively.

552 These results establish V_m fluctuations as an informative gauge of high-dimensional information, while
553 also demonstrating that the power-law characteristics are universal properties of the brain, by showing a close
554 match between data at different scales and under different conditions. Further underscoring universality, our
555 results are also similar to the critical exponents measured from other animals such as the $\tau = 1.8$ result from in-
556 vivo anesthetized cats (Hahn et al., 2010), though an exhaustive literature search was not conducted, others have
557 conducted incomplete surveys (Ribeiro et al., 2010; Priesemann, 2014).
558

559 **The Single-Neuron Estimate of Network Dynamics is Optimized at the Network Critical Point**

560 To gain a deeper insight into the relation between single-neuron input and network activity, we
561 investigated a model network of probabilistic integrate and fire model neurons (Kinouchi and Copelli, 2006;
562 Larremore et al., 2011a, 2011b, 2012, 2014, Karimipناه et al., 2017a, 2017b). This model network contains
563 fundamental features of cortical populations, such as low connectivity, inhibition, and spiking, while being
564 sufficiently tractable for mathematical analysis (see Methods: Model Simulations).

565 In brief, the model network consists of $N = 10^4$ binary probabilistic model neurons (**Figure 4A**). The
566 connection probability c results in a mean in-degree and out-degree of cN . The connection strength from neuron j
567 to neuron i is quantified in terms of the network adjacency matrix W . Each connection strength W_{ij} is drawn from
568 a distribution of (initially) positive numbers with mean η , where the distribution is uniform on $[0, 2\eta]$. A fraction χ
569 of the neurons are designated as inhibitory, i.e., their outgoing connections are made negative. The binary state
570 $S_i(t)$ of neuron i is updated according to $S_i(t) = \theta(\sum_j^N W_{ij} S_j(t-1) - \xi_i(t))$, where $\xi_i(t)$ is a random number
571 between 0 and 1 drawn from a uniform distribution, and θ is the Heaviside step function.

572 The largest eigenvalue $\lambda = \eta c N (1 - 2\chi)$ of the network adjacency matrix W , characterizes the network
573 dynamics, with critical network dynamics occurring at $\lambda = 1$. This tuning parameter λ controls the degree to which
574 spike propagation “branches”: $\lambda = 1$ means that one spike creates one other spike on average, $\lambda > 1$ implies that
575 one spike creates more than one other spike while $\lambda < 1$ means that one spike creates less than one other spike

576 (Haldeman and Beggs, 2005; Kinouchi and Copelli, 2006; Levina et al., 2007; Larremore et al., 2011b, 2012; Kello,
577 2013).

578 The input to model neuron i , is $P_i(t) = \sum_j^N W_{ij} S_j(t-1)$ and provides the link between network activity
579 and single-neuron activity. From this we can derive a simple mathematical result characterizing how estimation of
580 network properties is optimized at criticality.

581 If we let $K_i(t-1)$ denote the number of active neurons *in the presynaptic population* of neuron i , then
582 we can rewrite the input to a model neuron as a sum of independent and identically distributed random variables
583 drawn from the non-zero entries of W : $P_i(t) = \sum_k^{K_i(t-1)} W_{ijk}$. After implementing inhibition by inverting some
584 elements of W the distribution of weights is not uniform but piecewise uniform. Weights are drawn uniformly
585 from the interval $[-2\eta, 0]$ with probability χ and from the interval $[0, 2\eta]$ with probability $1 - \chi$. The mean of the
586 nonzero entries of W are denoted with a prime so that the mean is $\langle W'_{ij} \rangle = \eta(1 - 2\chi)$ and the standard deviation
587 is $\sqrt{\langle W_{ij}^2 \rangle - \langle W_{ij} \rangle^2} = \eta\sqrt{(1 - 12(\chi^2 - \chi))}/3$. Now we can find the mean behavior of the input integration
588 function as it relates to the presynaptic population:

$$589 \quad \langle P_i(t) \rangle \pm \sigma_{P_i(t)} = \eta(1 - 2\chi)K_i(t-1) \pm \eta\sqrt{(1 - 12(\chi^2 - \chi))}K_i(t-1)/3.$$

590 We learn three things by examining the mean behavior of the input integration function. First, the mean
591 grows as $O(K_i)$ but the standard deviation grows as the root $O(\sqrt{K_i})$, so the function becomes a more precise
592 estimator of network activity with increasing activity in the presynaptic population (increasing K_i). Second, the
593 input integration function $P_i(t)$, is rarely negative. At the parameter combination $c = 0.005$ and $\chi = 0.25$ (which
594 has the largest variance relative to the mean) the mean becomes more than one standard deviation larger than
595 zero when $K_i > 5$. Third, and most importantly, the input integration function is an averaging operator and the
596 tuning parameter λ biases that averaging operation. To show this we only need two observations: the
597 instantaneous firing rate averaged over the presynaptic population is the number of active neurons divided by the
598 expected total number of presynaptic neurons, $\omega_i(t) = K_i(t)/cN$. Next, we rearrange the definition of lambda to

599 get $\lambda/cN = \eta(1 - 2\chi)$. Substituting these two observations into the mean behavior of our input integration
 600 function we get the key mathematical result:

$$P_i(t) = \sum_j^N W_{ij} S_j(t-1) \sim \lambda \omega_i(t-1)$$

601 Note that $P_i'(t) = P_i(t) \times \Theta(P_i(t))$ directly represents the probability for the neuron to spike at time t .

602 These results demonstrate that the inputs to a neuron P_i , and the instantaneous firing rate of that neuron
 603 are the result of an averaging operator acting on the presynaptic population, which is a subsample of the network.
 604 Furthermore, the tuning parameter λ not only modulates the relationship of single neuron firing to downstream
 605 events (also known as branching), but also governs how the input to a neuron relates to the presynaptic
 606 population. It biases the averaging operator to either amplify firing rate ($\lambda > 1$) or dampen it ($\lambda < 1$). Therefore,
 607 our model implements both critical branching and the inverse of the critical branching condition, a *critical coarse-*
 608 *graining* condition. The model is a network of subsampling operators who only capture whole-system statistics
 609 when $\lambda = 1$ and the operators reflect an unbiased stochastic estimate of mean firing rate among the subsample
 610 (the presynaptic population). This averaging operation may exist in many kinds of networks, including those with
 611 structure and those that are not critical branching networks, so this result helps establish plausible generalizability.

612 To further evaluate the relation between single-neuron input and network activity under different
 613 conditions, we simulated the described network of 10^4 model neurons for a total of 405 different parameter
 614 combinations, including connection probability, inhibition, and maximum eigenvalue (**Figure 4A**), each parameter
 615 combination was repeated ten times. We then compared the avalanche analysis results of simulated network
 616 activity $F(t) = (\frac{1}{N}) \sum_{i=1}^N S_i(t)$ and the input to a single neuron (the input integration function). However,
 617 $P_i(t) = \sum_j^N W_{ij} S_j(t)$ is the probability that neuron i will fire at time t , also known as the instantaneous firing rate
 618 of neuron i .

619 Membrane potential is not a direct representation of firing rate, but rather the firing rate is related to
 620 synaptic input through the F-I curve which is non-linearly related to membrane potential. This non-linearity could
 621 destroy the correspondence between the simulated single neuron signal and network activity. In order to better

622 facilitate comparison of the simulated input integration function with the experimentally recorded membrane
623 potential, we constructed a proxy for the subthreshold membrane potential, $\Phi_i(t)$, of a model neuron by
624 convolving the simulated input $P_i(t)$ with an alpha function (see Methods: Model Simulations).

625 The parameter space has four distinct patterns of critical network behavior (**Figure 4B**). Qualitatively,
626 these were reflected in the network activity. As the presence of these paradoxical behaviors may indicate the
627 presence of second phase-transition tuned by the balance of excitation to inhibition (Shew et al., 2011; Poil et al.,
628 2012; Kello, 2013; Hesse and Gross, 2014; Larremore et al., 2014; Scarpetta et al., 2018) several key results differ
629 strongly and thus are reported separately for these regions of parameter space.

630 These regions are defined in terms of the connection density and inhibition and shown in **figure 4B**. First
631 is the “positive weights” region, there is no inhibition ($\chi = 0$) and the network is a standard critical branching
632 network. The second region, “quiet”, has a small increase in the fraction of inhibitory neurons. Activity lasts slightly
633 longer than for the classically critical network. The third region is called the “switching” regime because network
634 activity switches between a low mean and a high mean (like “up and down states” (Destexhe et al., 2003; Millman
635 et al., 2010; Larremore et al., 2014; Scarpetta et al., 2018)). This occurred in the middle portion of the values of
636 connectivity and inhibition. Lastly, we have the “ceaseless” region, with a large fraction of inhibition, relative to
637 connection density, activity never dies out. This region is defined by $c < (10e^{12\chi} - 13)/100$ and $\chi > 0$. Three of
638 these regimes are displayed in figure 5A, the “quiet” region is mostly redundant to the “positive weights” region.
639 The “ceaseless” and “switching” regimes exhibit sustained self-generated activity and is included with the intention
640 to model ongoing spontaneous activity dynamics without contamination by externally imposed firing patterns
641 (Mao et al., 2001).

642 We looked at the magnitude of relative error between estimated exponents for the avalanche size
643 distribution (**Figure 4C**) to determine how well our proxy neural inputs, $\phi_i(t)$, reflected network activity, $F(t)$, in
644 different parameter regions, and with different values for the tuning parameter, λ . Importantly the least error
645 occurred for $\lambda = 1$ with and without the presence of inhibitory nodes. This insensitivity to parameter differences
646 supports the claim (Larremore et al., 2014) that the system becomes critical when $\lambda = 1$ even in the presence of
647 inhibition.

648 However, the four regions of parameter space perform differently according to our four standardized
649 criteria for consistency with criticality. In the “positive weights” region 90% of 90 trials (nine points in parameter
650 space with ten trials per point) have network activity that meets all four criteria when the tuning parameter is set
651 at criticality ($\lambda = 1$) (**Figure 4C**). Meanwhile 39% meet the criteria in the “ceaseless” region, 19% do in the “quiet”
652 region, and 67% do in the “switching” region which may indicate the location of a second phase-transition and
653 shows that evidence for precise criticality in this model is limited once inhibition is included.

654 As we vary the tuning parameter, we can clearly distinguish critical from non-critical systems. Over all 47%
655 percent of trials meet all four criteria when $\lambda = 1$, while 3% do when $\lambda = 0.95$, 18% do when $\lambda = 1.015$, 1% do
656 when $\lambda = 0.9$, and 1% do when $\lambda = 1.03$ (**Figure 4D**).

657 The estimated power-law exponents show that the avalanche size distributions for $F(t)$, $P_i(t)$, and $\Phi_i(t)$
658 are most alike at criticality. Note that estimated exponents serves as the “scaling index”, a measure of the heavy
659 tail even when a power-law is not the statistical model that fits best (Jeżewski, 2004). The fact that matching
660 between network activity and the input integration function was best at criticality is important because it
661 underscores the scale-free nature of critical phenomena and contrasts with the results obtained when testing a
662 different relationship between subsampling methods and network structure (Priesemann et al., 2009; Yu et al.,
663 2014; Levina and Priesemann, 2017).

664 While the system was both critical ($\lambda = 1$) and in the positive weights region, our V_m proxy $\Phi_i(t)$ met all
665 four criteria for consistency with criticality 74% of the time for 90 trials (**Figure 4D**) while $P_i(t)$ met all four only 1%
666 of the time. The network activity had avalanche size and duration exponent values $\tau_F = 1.43 \pm 0.04$, and
667 $\beta_F = 1.87 \pm 0.09$, (**Figure 4D**) and had a fitted scaling relation exponent, $\gamma_{F_f} = 1.83 \pm 0.02$, and a predicted
668 exponent $\gamma_{F_p} = 1.99 \pm 0.23$. The membrane potential proxy, $\Phi_i(t)$ had slightly lower avalanche size and duration
669 exponent values that fluctuated around the paired network values, $\tau_\Phi = 1.40 \pm 0.06$, and $\beta_\Phi = 1.73 \pm 0.17$,
670 (**Figure 4D**) and exclusively lower scaling relation exponents $\gamma_{\Phi_f} = 1.68 \pm 0.02$. While the unsmoothed $P_i(t)$
671 varied considerably more it had size and duration exponents that were almost exclusively higher than the paired

672 network values, $\tau_p = 1.87 \pm 0.50$, and $\beta_p = 2.84 \pm 1.45$, with a fitted scaling relation exponent that was
673 exclusively lower $\gamma_{P_f} = 1.68 \pm 0.02$.

674 In figure 5, we compared different population dynamics estimation techniques by looking at avalanches
675 inferred from $P_i(t)$ (the inputs to neuron i), and the V_m proxy $\Phi_i(t)$. Both $P_i(t)$ and $\Phi_i(t)$ fluctuate about $F(t)$
676 but $P_i(t)$ is much noisier (**Figure 5A**), in the ceaseless regime $P_i(t)$ and $\Phi_i(t)$ are systematically offset. Avalanches
677 inferred from $\Phi_i(t)$ had average sizes that scaled with duration (**Figure 5B**). Avalanches from $\Phi_i(t)$ consistently
678 had duration and size distribution exponents that were closer to network avalanches than avalanches from $P_i(t)$.
679 However, $P_i(t)$ performed satisfactorily in the sense that its error was systematically offset and best at criticality
680 (**Figure 5C**).

681 Including inhibition introduces several important differences. For the ceaseless region with $\lambda = 1$, far
682 fewer trails meet our criteria, however $P_i(t)$ follows $F(t)$ much more closely. The network activity had avalanche
683 size and duration exponent values $\tau_F = 1.48 \pm 0.09$, and $\beta_F = 1.53 \pm 0.09$, and had a fitted scaling relation
684 exponent, $\gamma_{F_f} = 1.23 \pm 0.11$. The membrane potential proxy, $\Phi_i(t)$ had slightly higher avalanche size and
685 duration exponent values that fluctuated around the paired network values, $\tau_\Phi = 1.51 \pm 0.19$, and $\beta_\Phi = 1.57 \pm$
686 0.17 , but nearly identical scaling relation exponents $\gamma_{\Phi_f} = 1.23 \pm 0.11$. While the unsmoothed $P_i(t)$ varied
687 considerably more, it had size and duration exponents that were almost exclusively higher than the paired network
688 values, $\tau_p = 1.88 \pm 0.20$, and $\beta_p = 2.18 \pm 0.34$, with a fitted scaling relation exponent that was slightly lower
689 $\gamma_{P_f} = 1.19 \pm 0.07$.

690 When $\lambda \neq 1$ both $\Phi_i(t)$, and $P_i(t)$ failed to meet all four criteria for criticality at the same high rate as
691 $F(t)$ (to within 1%). This lack of false positives confirms that these signals are useful for characterizing critical
692 branching. In figure 4, panel B, we calculated the absolute magnitude of relative error between the size exponent
693 from avalanche analysis performed on $F(t)$ and $\Phi_i(t)$. As expected, the avalanches were usually not power-laws
694 according to our standards, in this case the exponent is known as the “scaling index” and describes the decay of
695 the distribution’s heavy tail (Jeżewski, 2004).

696 When we set $\lambda = 0.95$ we see a moderate deterioration in the ability of either $\Phi_i(t)$ or $P_i(t)$ to
697 recapitulate network exponent values. The error is no longer systematic; thus, they cannot be used to predict
698 network values. The variability of the exponents increases greatly for $\Phi_i(t)$ while it decreases for $P_i(t)$. The
699 exponent error increases slightly over the $\lambda = 1$ and the base of the distribution is much broader.

700 Reducing λ further, to $\lambda = 0.90$, the input integration function, $P_i(t) \sim \lambda \omega_i(t - 1)$, rapidly dampens
701 impulses (ω_i is the instantaneous firing rate over the presynaptic population for neuron i). Variability continues to
702 increase, and a systematic offset does not return. Exponent error is now much broader. With branching this low,
703 events often are not able to propagate to the randomly selected neuron, an exception is the “ceaseless” regime
704 where activity is still long lived.

705 When we set $\lambda = 1.015$ we see a dramatic deterioration in the ability of either $\Phi_i(t)$ or $P_i(t)$ to
706 recapitulate network values. Variability in exponent estimation increases for both $\Phi_i(t)$ and $P_i(t)$. Exponent error
707 increases rapidly, underscoring the inability to estimate network activity from neuron inputs.

708 Increasing λ further to $\lambda = 1.03$ produces an input integration function, $P_i(t) \sim \lambda \omega_i(t - 1)$, that rapidly
709 amplifies all impulses and the network saturates. The effect is that variability in the estimated exponents
710 decreases and a systematic offset returns, with both $\Phi_i(t)$ and $P_i(t)$ producing exponents that are exclusively and
711 considerably higher than network values. Exponent error reveals that estimating network properties from the
712 inputs to a neuron is probably not possible for supercriticality in this model.

713 The results here show that the V_m proxy represents an effective way of subsampling network flow. This is
714 a hallmark of the near-critical region in the PIF model and a manifestation of scale-freeness. Criticality in our model
715 corresponds to the point when the inputs to a neuron represent an average of the activity of the presynaptic
716 population. Importantly we explored why it works, as well as showing that it does work in experimental data. This
717 analysis, presented in forthcoming sections, uncovered that proper temporal and spatial aggregation is important
718 as is the role of inhibition in membrane potential dynamics. This supports both the criticality hypothesis, and tight
719 balance (Barrett et al., 2013; Boerlin et al., 2013; Denève and Machens, 2016). Additionally, it has specific

720 implications for the information content of membrane potential.

721

722 **The Predicted Scaling Relation Exponent is More Stable than Avalanche Size or Duration Exponents**

723 A key part of the study of criticality in neural systems is the assumption that biological systems must self-
724 organize to a critical point. The precise critical point is a very small target for a self-organizing mechanism in any
725 natural system. So, a key question is whether the self-organizing mechanism of the brain prioritizes efficiently
726 achieving information processing advantages of scale-free covariance at the expense of being slightly sub or super-
727 critical (which is a larger target) (Priesemann, 2014; Tomen et al., 2014; Williams-García et al., 2014; Gautam et al.,
728 2015; Clawson et al., 2017).

729 Our data offered unexpected insight. It is known that so long as three requirements are met the scaling
730 relation will be marginally obeyed: Avalanche size and durations must be power-law distributed (with exponents τ
731 and β respectively) and average size must scale with duration according to a power-law with exponent γ . Given
732 those three requirements one can derive a prediction for the scaling exponent, $\gamma_p = (\beta - 1)/(\tau - 1)$ without
733 needing to assume criticality (Scarpetta et al., 2018). However, without any other assumptions one expects β and τ
734 to be independent so plotting one against the other should make a point-cloud that is symmetrical, not stretched
735 along a trendline (**Figure 3**).

736 We analyzed the independence of τ , β , and γ measured from experimental data (where self-organization
737 is hypothesized) and compared it to model data (where self-organization is impossible, but criticality is
738 guaranteed). We found that β and τ are more independent and the predicted scaling relation is more variable for
739 the model than for experimental data in which β and τ covary, apparently in order to maintain a fixed scaling
740 relation prediction.

741 The previous multi-site LFP recordings displayed a range of values for the avalanche size τ and duration β
742 distribution exponents across the tested brain preparations. Interestingly, the exponent values were not
743 independent, rather the duration exponent varied linearly with the size exponent (Shew et al., 2015) (**Figure 3A**).
744 The single-neuron V_m fluctuations, reported here, produced a similar linear relationship between size and duration

745 exponent (**Figure 3B**). Algebraic manipulation of the predicted scaling exponent $\gamma_p = (\beta - 1)/(\tau - 1)$ provides
 746 a clue. If the scaling relation $(\beta - 1) = \gamma(\tau - 1)$ is obeyed and if γ_p is a *fixed universal property*, then the linear
 747 relationship $\beta_j \propto \langle \gamma_p \rangle \tau_j$ holds across different cells and animals.

748 To demonstrate this important result, variability in the predicted scaling-relation is much less than
 749 expected, we propagate errors and assume independent β and τ . We would expect the standard deviation of γ_p to
 750 be $\sigma_{\gamma_p}^* \sim \frac{|\beta-1|}{|\tau-1|} \sqrt{\left(\frac{\sigma_\beta}{\beta-1}\right)^2 + \left(\frac{\sigma_\tau}{\tau-1}\right)^2} \sim 0.72$ which is roughly twice the real value in V_m data, $\sigma_{\gamma_p} \sim 0.35$.

751 Pearson correlation, ρ , confirms strong dependence between τ and β , $\rho_{\tau\beta} = 0.61$, p-value $p = 2.57 \times$
 752 10^{-6} for the V_m data while for the MEA data $\rho_{\tau\beta} = 0.96$, p-value $p = 1.01 \times 10^{-7}$. From this we confirm what
 753 figure 3 shows: the variability in τ and β are not independent and this implies the existence of an organizing
 754 principle connecting τ to β . Whatever the principle may turn out to be, one of its effects is the maintenance of
 755 low variability in γ_p at the expense of greater variability in τ and β .

756 A principle reason to suspect self-organization is that this trend is not seen in the model results.
 757 Importantly, τ and β are independent of the scaling-relation exponent function, though still weakly correlated. In
 758 this model there is no adaptive organizing principle driving this network to criticality, instead the structure is fixed
 759 and set to be at the critical point. This shows how systems behave in the absence of self-organization. No
 760 parameter is being maintained at low variability at the expense of other parameters.

761 Limiting ourselves to simulated network activity for the $\lambda = 1$ case without inhibition (**Figure 4C**),
 762 propagation of errors leads us to expect the standard deviation of the scaling-relation prediction to be $\sigma_{\gamma_{FP}}^* \sim 0.27$
 763 which is very close to real value $\sigma_{\gamma_{FP}} \sim 0.23$. The correlation is statistically significant at the 5% level, but much
 764 smaller $\rho_{\tau\beta} = 0.23$, p-value $p = 0.027$.

765 This was noted in the original paper (Shew et al., 2015) where they were able to reproduce the linear
 766 trend between avalanche size and duration exponents by simulating a network with synaptic depression to
 767 adaptively restore critical behavior after an increase in network drive. They show that the trendline is produced by
 768 corrupting their simulated data via randomly deleting seventy to ninety percent of spiking events and then

769 changing the way they group events in time (adaptive time binning). Our membrane potential fluctuations have no
770 counterpart to the adaptive time binning other than the intrinsic membrane time constant which is not
771 manipulated experimentally.

772 In conclusion, the linear trend between avalanche size and duration exponents is not a universal property
773 of critical systems because it was not found in the model. This suggests that the linear trend is enforced by an
774 organizing principle at work in the brain but absent in the model. This principle prioritizes maintaining stability in
775 either the scaling of avalanche size with duration, or the power-law scaling of autocorrelation which is closely
776 related to the scaling relation and scale-free covariance via the power-law governing auto-correlation (Bak et al.,
777 1987; Sethna et al., 2001).

778

779 **Non-Linearity and Temporal Characteristics such as High-Order Correlation, Proper Combination of Synaptic**
780 **Events, and Signal Time-Scale are Required to Reproduce Network Measures from Single-Electrode Recordings**

781 In order to demonstrate that subthreshold membrane potential fluctuations can be used as an
782 informative gauge of cortical population activity it is necessary to compare against alternative signals which have
783 either been used by experimentalists as a measure of population activity or that share some key features of
784 membrane potential but are missing others. By making these comparisons we can illuminate which features of the
785 membrane potential signal are responsible for its ability to preserve properties of cortical network activity.
786 Additionally, it is necessary to check whether the statistical properties of avalanches can be explained by random
787 processes unrelated to criticality. To address these points of the investigation, we analyzed five surrogate signals:
788 single-site LFP recorded concurrently with the V_m recordings, two phase-shuffled versions of V_m recordings,
789 computationally inferred excitatory current, and the same inferred excitatory current further transformed to
790 match V_m autocorrelation (which tests the role of IPSPs by making a V_m -like signal that lacks them).

791 **Negative fluctuations of LFP disagree with V_m and MEA results and are inconsistent with avalanches in**
792 **critical systems.**

793 The first alternative hypothesis to test is whether the LFP could yield the same results. We used low-pass
794 filtered and inverted single site local field potential (LFP) which is commonly believed to measure local population
795 activity. However, in our analysis it did not recapitulate the results from either MEA or V_m avalanche analysis. We
796 obtained viable single-site LFP recordings (see Methods: Extracellular Recordings), simultaneous and adjacent with
797 whole-cell recordings, for 38 of the 51 neurons reported above. We performed avalanche analyses on the LFP
798 recordings using a procedure like the one described for the V_m recordings (see Methods: Intracellular Recordings)
799 (**Figure 6**). LFP recordings were grouped the same way V_m recordings were in order to match them for comparison.
800 However, the numbers of recordings are not the same because there were two or three cells being patched
801 alongside (within $300 \mu m$) one extracellular electrode and there was not always a simultaneous LFP recording. LFP
802 also produced more avalanches per 2-5-minute recording $N_{AV} = 1128 \pm 348$. There are 23 20-minute periods
803 spanning multiple LFP recordings. These recordings were gathered into groups and matched against 49 V_m
804 recording groups (38 from the first 20-minute period, 11 from the second). Additionally, there were 16 20-minute
805 periods spanning only one LFP recording but with more than 500 avalanches. The concurrent V_m recordings did not
806 have enough avalanches. This gives us 39 LFP avalanche data sets.

807 The LFP recording groups performed poorly according to our four criteria for consistency with criticality.
808 Of the 39 LFP recording groups, only 41% percent had acceptable scaling relation predictions and only 36% met all
809 four standard criteria for criticality (**Figure 7A**). The additional criterion of shape collapse was not observed (**Figure**
810 **6C**), there was no linear trend among the exponents governed by the scaling relation and the exponents did not
811 match MEA data (**Figure 3A**). However, 85% produced power-law fits for size and duration, 92% had scaling
812 relations well fit by power-laws and all were non-trivial. We expect from (Touboul and Destexhe, 2017) that some
813 fraction of non-critical data will pass the four standard criteria by chance, so long as the data have a $1/f$ power
814 spectrum.

815 To emphasize that these results are chance we can limit ourselves to just those with the best chance of
816 meeting the scaling relation criteria by picking those that have power-laws in the size and duration distributions.
817 This is enough to expect the scaling relation to be obeyed if mean size scales geometrically with duration
818 (Scarpetta et al., 2018). It is still the case that only 42% of recording groups meet the three remaining standard

819 criteria for consistency with criticality. Therefore, having power-laws is statistically independent of meeting the
820 other criterion for consistency with criticality.

821 Not only does the single-site LFP data differ from MEA and V_m data because it fails to demonstrate
822 consistency with criticality, it is also the case that the scale-free properties which do exist are not representative of
823 the MEA data or the simultaneous V_m recordings. The failure was not because LFP recordings co-occurred with
824 decreased consistency with criticality more generally. Eighty-one percent of the matched V_m recordings met all the
825 criteria, while 58% of the LFP recordings did, a statistically significant dissimilarity, odds ratio ($r_{OR} = 7.65$ with
826 $p = 1.1 \times 10^{-5}$).

827 The estimated exponents from all 39 LFP recording groups were highly variable. The duration distribution
828 and scaling relation were most dissimilar to V_m and MEA data. Of the 33 LFP groups which were power-law
829 distributed, the avalanche size exponent had a median value $\tau = 1.90 \pm 0.63$ while the duration exponent was
830 $\beta = 1.41 \pm 0.9$ (very low) (**Figure 7A**) and the fitted exponent was $\gamma_f = 1.11 \pm 0.02$. The predicted scaling-
831 relation exponents were inaccurate with $\gamma_p = 0.89 \pm 0.76$ for the subset of recording groups which had power-
832 laws.

833 The extreme variability makes it hard to determine whether the size and duration exponents match other
834 data, but the fitted scaling relation exponent was much less variable and more clearly separated from MEA or V_m
835 results. The matched difference of median test (Wilcoxon signed-rank) between 49 recording groups found that
836 the best fit τ ($\tau = 1.90 \pm 0.63$) was not significantly distinguishable from the V_m data ($r_{SDF} = 0.15, p = 0.33$),
837 but β ($\beta = 1.41 \pm 0.9$) was dissimilar with a comparable effect size ($r_{SDF} = 0.17, p = 0.028$), and γ_f ($\gamma_f = 1.11 \pm$
838 0.02) was also dissimilar ($r_{SDF} = 0.25, p = 7.1 \times 10^{-15}$).

839 When comparing to the 13 samples of MEA data γ_f was significantly different from the MEA data
840 ($r_{SDF} = 0.88$, and $p = 9.21 \times 10^{-08}$). This contrasts with our comparison between V_m and MEA data. In that case
841 the scaling relation was not distinguishable even with 51 points of comparison and very low variability making a
842 difference easier to detect. However, because of their extreme variability the size and duration exponents fail a 5%
843 significance threshold for distinguishing from the MEA data by a Wilcoxon rank-sum result ($r_{SDF} = 0.06, p = 0.766$

844 for τ and $r_{SDF} = 0.29, p = 0.123$ for β). This failure of inverted LFP to show the same statistical properties as
845 multi-unit activity may add a caveat to the assumptions behind the use of inverted LFP as a proxy for population
846 activity (Kelly et al., 2010; Einevoll et al., 2013; Okun et al., 2015). Specifically, the amplitude of *single-electrode*
847 negative LFP excursions is ambiguously related to the number of spiking neurons, whereas the use of electrode
848 arrays as in (Beggs and Plenz, 2003) and in (Shew et al., 2015) is more appropriate.

849 To summarize, the single-site LFP fluctuation results from the superposition of local spiking and
850 extracellular synaptic current of juxtaposed network elements (Kajikawa and Schroeder, 2011; Einevoll et al., 2013;
851 Pettersen et al., 2014; Ness et al., 2016). These fluctuations were found to be less informative about the network
852 dynamics than single-neuron V_m fluctuations. V_m fluctuations result from the superposition of EPSPs and IPSPs
853 indicating neuronal responses propagating in a manner consistent with the true neural network architecture. In
854 other words, synaptic and spiking events driving fluctuations at single extracellular electrodes may be too badly
855 out of sequence and distorted to faithfully represent neuronal avalanches, whereas the sequence of synaptic and
856 spiking events driving somatic membrane potential fluctuations is functionally relevant by definition.

857

858 **Stochastic surrogates are distinguishable from V_m or MEA results, reveal importance of non-linear**
859 **filtering.**

860 After eliminating inverted LFP as an alternative single-electrode signal, it was important to establish
861 whether our results could have been created from a linear combination of independent random processes
862 (Touboul and Destexhe, 2017; Priesemann and Shriki, 2018), similar to those used when contesting evidence for
863 critical brain dynamics (Bédard et al., 2006; Touboul and Destexhe, 2010, 2017). We also wanted to learn what
864 effects non-linearity (non-Gaussianity) has in signals like the V_m .

865 To address these questions, we used both the AAFT and UFT phase shuffling algorithms (see Methods:
866 Experimental Design and Statistical Analysis). AAFT (**Figure 6**) preserves both the exact power-spectrum
867 (autocorrelation) of the signal and non-linear skew of signal values but randomizes the phase (higher-order
868 temporal correlations). UFT is the same but forces the distribution of signal values to be Gaussian. Using both

869 allows us to attribute some characteristics to non-linear rescaling and others to precise temporal correlation
870 structure.

871 Phase shuffling tends to preserve power-laws since it explicitly preserves the $1/f$ trend of the power-
872 spectrum. However, the matched signed-rank test reveals that the values of the exponents change in both
873 methods. Under UFT transformation the scaling relation and shape collapse became more trivial and like the LFP.
874 This suggests that both the non-linear rescaling of input currents by membrane properties and the way that input
875 populations interact throughout the intricate dendritic arborization are important.

876 For the 51 recording groups from the first 20-minutes the AAFT reshuffled data yield a median size
877 exponent of $\tau = 1.74 \pm 0.29$ while the duration exponent was $\beta = 2.0 \pm 0.34$ (**Figure 7D**). The fitted scaling
878 relation exponent was $\gamma_f = 1.19 \pm 0.06$ and the predicted scaling relation exponent was $\gamma_p = 1.21 \pm 0.49$.

879 Pairing the surrogates to the original V_m data and performing the Wilcoxon signed-rank test for difference
880 of medians gives ($r_{SDF} = 0.053$, $p = 2 \times 10^{-4}$), ($r_{SDF} = 0.091$, $p = 0.08$), and ($r_{SDF} = 0.207$, $p = 3 \times 10^{-5}$) for
881 τ , β , and γ_f respectively. Thus τ and γ_f are both significantly different, this is supported by the fact that only 55%
882 of the groups meet all four standard criteria for criticality, while 76% of meet them for the original V_m time series.
883 This difference between success rates is significant by Fisher's exact test ($r_{OR} = 2.67$, $p = 0.0363$).

884 The failure mode for AAFT shuffled data was almost entirely in reduced goodness of fit (R^2) for a power-
885 law fit to its scaling relation, 17% fewer recording groups met the criterion $R^2 > 0.95$, than for V_m ($r_{OR} =$
886 4.18 , $p = 0.0093$). When the shape collapse is examined, we see another clear, if qualitative, difference in the
887 symmetry of any presumed scaling function (**Figure 6C**). When taken together can we see that the AAFT shuffled
888 dataset is not consistent with critical point behavior. Thus, we show that the exponent values and evidence for
889 criticality, especially scaling and shape collapse which we inferred from V_m are not likely to come from random
890 processes and are dependent on non-linear temporal correlation structure.

891 The key feature of the UFT result is that the fitted scaling relation exponent is much lower, $\gamma_f = 1.05 \pm$
892 0.049 , which is significantly less than for AAFT ($r_{SDF} = 0.25$, $p = 1 \times 10^{-13}$) and less than the LFP ($r_{SDF} =$
893 0.228 , $p = 3 \times 10^{-6}$). It is very close to trivial scaling but is still distinguishable from $\gamma_f = 1$ at a population level

894 via the sign test ($r_{SDF} = 0.843, p = 2 \times 10^{-10}$). Because the fitted scaling relation exponent and shape collapse
895 were similar in both the UFT and LFP data, it suggests that lack of non-linear rescaling (non-linear filtering) may be
896 a key feature of LFP that explains its failure to accurately reflect critical point behavior.

897 The UFT was universally poorer performing, 39% do pass the criticality test but given that the scaling
898 relation exponent is so low this is simply random chance, and significantly worse than the V_m results ($r_{OR} =$
899 $5.04, p = 3 \times 10^{-4}$). The UFT phase shuffling results obtain a median size exponent of $\tau = 1.69 \pm 0.45$ while the
900 duration exponent was $\beta = 1.81 \pm 0.49$. The predicted scaling relation exponent was $\gamma_p = 1.01 \pm 0.72$. All are
901 significantly different from the V_m results ($r_{SDF} = 0.183, p = 0.005$), ($r_{SDF} = 0.199, p = 2 \times 10^{-4}$), and
902 ($r_{SDF} = 0.249, p = 2 \times 10^{-13}$) for τ, β , and γ_f respectively. These results are redundant with the AAFT confirming
903 that our results do not have a trivial explanation.

904 When the scaling relation was examined, we saw another clear, if qualitative, difference in the symmetry
905 of any presumed scaling function (**Figure 6C**). When taken together, our four standardized criteria followed by
906 shape-collapse analysis let us distinguish phase-shuffled V_m fluctuations from the original V_m fluctuations, even
907 limiting ourselves to data that meets the four criteria. Thus, the phase-shuffled data showed that the evidence for
908 criticality in the original V_m fluctuations are dependent on non-linear temporal correlations.

909

910 **Excitatory and Inhibitory Synaptic Activity are Both Required for V_m Fluctuations to Match MEA Avalanches**

911 Having learned that single-site LFP recordings cannot be used to accurately infer the statistics of
912 population activity, and knowing that low-pass filtered and inverted LFP is believed to reflect *excitatory* synaptic
913 activity (Kajikawa and Schroeder, 2011; Buzsáki et al., 2012; Einevoll et al., 2013; Ness et al., 2016) it begs the
914 question: to what extent do excitatory synaptic events contain evidence for network criticality?

915 Somatic V_m fluctuations are the complex result of spatially and temporally distributed excitatory and
916 inhibitory synaptic inputs further mangled by active and passive membrane properties in dendrites and soma.
917 There is reason to believe that these features conspire to enforce the condition that V_m faithfully represents inputs
918 to the presynaptic network (Barrett et al., 2013; Boerlin et al., 2013; Denève and Machens, 2016) similar to how

919 input signals relate to presynaptic populations in our model. To address the stated question, we estimated the
920 excitatory synaptic conductance changes g_{exc}^* from the V_m recordings, using a previously developed inverse
921 modeling algorithm (Yaşar et al., 2016), and applied the avalanche analysis on the inferred g_{exc}^* time series, (**Figure**
922 **6**).

923 The inferred excitatory conductance is plausibly related to the presynaptic population, however it failed
924 to be a reliable measure of network dynamics (**Figure 7B**). We can't know whether the failure is because excitatory
925 current does not contain enough information or because the signal's time constant is too short. Power laws in the
926 avalanche size and duration distributions were observed in only 12% of the 51 groups from the first 20 minutes of
927 recording. Comparing to V_m this was very different ($r_{OR} = 375, p = 6 \times 10^{-14}$). Shape collapse was absent from
928 the inferred excitatory conductance (**Figure 6C**) and none passed all four criteria for criticality. From this we
929 conclude that inferred excitatory conductances are not a good network measure.

930 One of many potential reasons for this failure could be the much shorter time constant of the inferred
931 g_{exc}^* signal compared to the V_m signal. We saw exactly that situation when examining model results: $P_i(t)$ failed to
932 reproduce network values as well as its smoothed version $\phi_i(t)$. Therefore, we smoothed the g_{exc}^* signal with an
933 alpha-function, chosen because it should impose a similar non-Gaussian distribution as the V_m signal. The time
934 constant of the alpha function was tuned to minimize the error between the autocorrelation of the smoothed g_{exc}^*
935 signal and the original V_m signal. By doing so we create a signal with a $1/f$ power-spectrum that should exhibit
936 power-laws and reproduce many V_m statistical features, (**Figure 6**).

937 Reinstating the autocorrelation does not summon the return of scale-freeness. The smoothed signal did
938 demonstrate power-laws (94%) and one serendipitously met the standardized criteria for consistency with critical
939 point behavior (**Figure 6D**). However, this is chance. The average coefficient of determination for a fitted scaling
940 relation on a log-log plot was $R^2 = 0.84 \pm 0.14$ so overall average avalanche sizes did not scale with duration as a
941 power-law. Nonetheless this is a substantial improvement on the unsmoothed version $R^2 = 0.68 \pm 0.17$. This is a
942 statistically significant difference ($r_{SDF} = 0.054, p = 3 \times 10^{-4}$).

943 The smoothed inferred g_{exc}^* signal (**Figure 6A**) is visually more like the original V_m (**Figure 2B**) than the
944 AAFT shuffled V_m surrogate (**Figure 6A**), however, it was a worse match. This shows that signals dependent only on
945 excitation, even ones with the same non-Gaussian distribution and power-spectrum trend do not reflect the
946 statistics of population activity. Interactions between EPSPs and IPSPs may be needed.

947 In conclusion, the single-site local field potential (LFP), the phase-shuffled recorded V_m , and the inferred
948 excitatory conductance g_{exc}^* , including its smoothed version, all failed to reveal the critical network dynamics.
949 However, there are either similarities between the signals or some remaining scale-free signatures which reveal
950 the importance of signal aspects. In order to faithfully represent population activity statistics a candidate signal
951 must: have the right non-Gaussian distribution, the right $1/f$ power-spectrum characteristics and is sensitively
952 dependent on higher-order temporal correlations such as may result from the complex interplay of excitation and
953 inhibition within the dendritic arborization of a pyramidal neuron in the visual cortex.

954

955

Discussion

956 Leveraging membrane potential (V_m) and local field potential (LFP) recordings with modeling and
957 microelectrode array (MEA) data yielded two principle findings: subthreshold V_m are a useful indicator of network
958 activity and this correspondence is inherent to critical coarse-graining. Scrutiny revealed that avalanche size and
959 duration distribution parameters covary to maintain similar geometrical scaling across different experiments, a
960 noteworthy observation. The following discussion emphasizes possible significance and research intersections,
961 such as explaining disagreement with theory via subsampling effects or quasicriticality, or relating neural
962 computation to a mathematical apparatus within critical systems theory.

963 While “appropriating the brain’s own subsampling method” is a novel description of whole-cell
964 recordings, it was inspired by examples. Whole-cell recordings contain information about the network (Gasparini
965 and Magee, 2006; Mokeichev et al., 2007; Poulet and Petersen, 2008; El Boustani et al., 2009; Okun et al., 2015;
966 Malina et al., 2016; Hulse et al., 2017; Lee and Brecht, 2018) and stimulus (Anderson et al., 2000; Sachidhanandam
967 et al., 2013). Usually the focus is using neural inputs to predict outputs, not measuring population dynamics
968 (Destexhe and Paré, 1999; Carandini and Ferster, 2000; Isaacson and Scanziani, 2011; Okun et al., 2015).
969 Additionally, long-time or large-population statistics, like our avalanche analysis, are useful for understanding
970 neural code (Sachdev et al., 2004; Churchland et al., 2010; Crochet et al., 2011; Graupner and Reyes, 2013;
971 McGinley et al., 2015; Gao et al., 2016) and are robust to noise. Our finding that single V_m recordings reflect scale-
972 free network activity is significant as recording stability in behaving animals improves (Poulet and Petersen, 2008;
973 Kodandaramaiah et al., 2012; Lee and Brecht, 2018). We open the door to using V_m fluctuations as windows into
974 network dynamics.

975 Rigorous analysis supports our experimental conclusion: subthreshold V_m fluctuations mimic neuronal
976 avalanches and evince critical phenomena but negative LFP deflections don’t, despite being purported network
977 indicators (Bédard et al., 2006; Liu and Newsome, 2006; Kelly et al., 2010; Einevoll et al., 2013; Okun et al., 2015).
978 We invoke network not single-neuron criticality (Gal and Marom, 2013; Taillefumier and Magnasco, 2013) because
979 the trend between size and duration exponents agrees with MEA data. Our findings originate from spontaneous
980 activity of ex-vivo turtle visual cortex which shares many connectivity and functional features with mammalian

981 cortex (Ulinski, 1990; Larkum et al., 2008). Lastly, the results are not serendipitous noise because the V_m dataset
982 significantly differed from a dataset of phase-shuffled and rescaled surrogates (Theiler et al., 1992).

983 Readers keen on critical phenomena may notice our exponents differ from the exact theoretical
984 predictions ($\tau = 1.5$, $\beta = 2$ (Haldeman and Beggs, 2005)). Others observing this mismatch have suggested the
985 brain operates slightly off-critical (Hahn et al., 2010; Priesemann, 2014; Tomen et al., 2014).

986 An extension of this suggestion, quasicriticality (Williams-García et al., 2014), also explains the highly
987 stable scaling relation: biological systems blocked from precise criticality may optimize properties which are
988 maximized only for critical systems, becoming “quasicritical”. Correlation time and length are maximized only at
989 criticality and closely related to avalanche geometrical scaling (Tang and Bak, 1988; Sethna et al., 2001). If brains
990 optimize correlation length, a highly stable scaling relation may result. Furthermore, including inhibition
991 (Larremore et al., 2014) makes our otherwise critical model less consistent with criticality except that population
992 statistics can still be inferred from input fluctuations. The stable-scaling was not in the model, which lacks any
993 plasticity mechanisms. Stable-scaling may be a rare observation of self-organization principles such as
994 quasicriticality. A contributing explanation is subsampling effects (Priesemann et al., 2009; Levina and Priesemann,
995 2017) but it doesn’t explain the stable scaling relation unless quasicriticality is also invoked.

996 **Neuronal Avalanche and Neural Input Fluctuation Similarity is Captured by a Critical Recurrent Coarse-Graining** 997 **Network**

998 Our main modeling finding, inputs to a neuron reflect network activity best for critical branching
999 networks, is supported by a parameter sweep and detailed analysis. Our network had no structure, but structure
1000 exists at all scales of brain networks (Song et al., 2005; Perin et al., 2011; Shimono and Beggs, 2015) and can have
1001 profound impacts on network dynamics (Litwin-Kumar and Doiron, 2012; Mastrogiuseppe and Ostojic, 2018). We
1002 derived a relationship showing that the findings may be transferrable to networks where neural inputs fluctuate
1003 about proportionality to some subsample’s activity. We tune proportionality to be one, but that can also emerge
1004 from plasticity (Shew et al., 2015; Del Papa et al., 2017). Tight-balance suggests a biological mechanism causing
1005 subthreshold V_m to track excitation into a presynaptic population because IPSPs can have their timing and strength

1006 “balanced” to truncate EPSPs which would otherwise last longer than spurts of presynaptic excitation (Barrett et
1007 al., 2013; Boerlin et al., 2013; Gatys et al., 2015; Denève and Machens, 2016). We use V_m proxy, $\phi_i(t)$, an alpha
1008 function convolved with a point process, $P_i(t)$. This $\phi_i(t)$, is more like V_m than $P_i(t)$ and reproduces our
1009 experimental findings. Lastly, we investigate quasicriticality by including inhibition but tuning the maximum
1010 eigenvalue to what would be the critical point without inhibition.

1011 Our model provides insights on network subsampling and renormalization group. Usually subsampling
1012 means selecting neurons at random or modeling an MEA with an arbitrary grid (Priesemann et al., 2009). Our
1013 “subsample” is the presynaptic population represented by summing weighted inputs from active neurons. This is
1014 the first analysis intersecting network convergence (i.e. postsynaptic soma).

1015 Subsampling distorts avalanche size and duration, likely creating differences between experimental
1016 results and theoretical predictions (Priesemann et al., 2009; Ribeiro et al., 2014; Levina and Priesemann, 2017;
1017 Wilting and Priesemann, 2018). Subsampling may explain disagreement between avalanche analysis on simulated
1018 network activity, $F(t)$, V_m proxy $\phi_i(t)$, and single-neuron firing rate $P_i(t)$. However, V_m and MEA results are off
1019 theory but match each other. Either their subsampling errors are alike enough to produce similar distortions, or
1020 subsampling co-occurs with quasicriticality (Priesemann, 2014; Williams-García et al., 2014).

1021 Intriguingly, the Restricted Boltzmann Machine (RBM) (Aggarwal, 2018), (a related model) was exactly
1022 mapped to a “renormalization group” (RG) operator (Mehta and Schwab, 2014; Koch-Janusz and Ringel, 2018). RG
1023 is a mathematical apparatus relating bulk properties to minute interactions (Maris and Kadanoff, 1978; Nishimori
1024 and Ortiz, 2011; Sfondrini, 2012). It characterizes critical points of phase-transitions (Stanley, 1999; Sethna et al.,
1025 2001) and helps derive neuronal avalanche analysis predictions (Sethna et al., 2001; Le Doussal and Wiese, 2009;
1026 Papanikolaou et al., 2011; Cowan et al., 2013). RG operators coarse-grain and then rescale, like resizing a digital
1027 image. Crucially, iterating an appropriate operator on a critical system produces statistically identical “copies”, but
1028 on non-critical systems the iterations diverge. Our model averages (coarse-grains) presynaptic pools to get an
1029 instantaneous firing probability for each neuron. Then a logical operation (rescaling) sets the spiking states for the
1030 next iteration, demonstrating an RG-like operation that reproduces our experimental findings. Denève and
1031 Machens (2016) proposed a similar relationship between real V_m and presynaptic pools. The finding that a similar

1032 neural operation emerges in RBMs underscores the relevance of RG and the extension of our findings to structured
1033 or non-branching networks. The importance is that a recurrent coarse-graining network may be like a scale-free
1034 ouroboros, displaying widespread scale-freeness if any component is critical or briefly driven by critical or scale-
1035 free inputs (Mehta and Schwab, 2014; Schwab et al., 2014; Aoki and Kobayashi, 2017; Koch-Janusz and Ringel,
1036 2018).

1037 Significantly, associating neuronal processing with critical branching may induce an organizing principle,
1038 the “Information Bottleneck Principle”. This balances dimensionality reduction (compression) against information
1039 loss (Tishby and Zaslavsky, 2015) and is reminiscent of efficient coding (Friston, 2010; Denève and Machens, 2016),
1040 and origins of tuning curves (Wilson et al., 2016; Heeger, 2017). Koch-Janusz and Ringel (2018) trained their
1041 network by maximizing mutual information between many inputs and few outputs. This produced nodes with
1042 receptive fields matching popular RG operators. They derived correct power-laws by iterating the network.
1043 Applications of RG to neural computation are known: image processing (Gidas, 1989; Mehta and Schwab, 2014;
1044 Saremi and Sejnowski, 2016), brain and behavior (Freeman and Cao, 2008), emergent consciousness (Werner,
1045 2012; Fingelkurts et al., 2013; Laughlin, 2014), and hierarchical modular networks (Lee et al., 1986; Willcox, 1991)
1046 important for criticality (Moretti and Munoz, 2013). Furthermore, our model’s RG-like features are crucial to
1047 reproducing experimental results. It follows that elegant RG operators like in the RBM might also capture biological
1048 neuronal processing, fulfilling the demand for beautiful neuroscience models (Roberts, 2018) while offering
1049 insights into organizing principles and scale-freeness.

1050 **Conclusion**

1051 We established that subthreshold fluctuations of V_m in single neurons agree with neuronal avalanche
1052 statistics and with critical branching but fluctuations in other single-electrode signals do not. Computational
1053 modeling showed that accurate inference requires critical branching like connectivity. Fluctuation size scales with
1054 duration more self-consistently in experimental than model results, hinting at self-organization. These findings are
1055 consistent with a nascent reduction of neural computation to coarse-graining operations which may explain the
1056 prevalence of critical-like behavior during spontaneous neural activity. Fully articulating the implications requires
1057 more investigation, but we have substantially extended the evidence for critical phenomena in neural systems

1058 while rigorously demonstrating that subthreshold V_m fluctuations of single neurons contain useful information

1059 about dynamical network properties.

1060

References

- 1061 Aggarwal CC (2018) *Neural Networks and Deep Learning: A Textbook*. Springer International Publishing. ISBN: 978-
1062 3-319-94462-3.
- 1063 Anderson J, Lampl I, Reichova I, Carandini M, Ferster D (2000) Stimulus dependence of two-state fluctuations of
1064 membrane potential in cat visual cortex. *Nat Neurosci* 3:617–621 doi: 10.1038/75797.
- 1065 Aoki K-I, Kobayashi T (2017) Restricted Boltzmann Machines for the Long Range Ising Models. *Mod Phys Lett B*
1066 30:1650401 doi: 10.1142/S0217984916504017.
- 1067 Arviv O, Goldstein A, Shriki O (2015) Near-Critical Dynamics in Stimulus-Evoked Activity of the Human Brain and Its
1068 Relation to Spontaneous Resting-State Activity. *J Neurosci* 35:13927–13942 doi: 10.1523/JNEUROSCI.0477-
1069 15.2015.
- 1070 Bak P, Tang C, Wiesenfeld K (1987) Self-organized criticality: An explanation of the 1/f noise. *Phys Rev Lett* 59:381–
1071 384 doi: 10.1103/PhysRevLett.59.381.
- 1072 Barrett D, Denève S, Machens C (2013) Firing rate predictions in optimal balanced networks. In: *Advances in Neural*
1073 *Information Processing (NIPS)* (Pereira F, Burges CJC, Bottou L, Weinberger KQ, eds), pp 1–9. Curran
1074 Associates, Inc. ISBN: 9781632660244.
- 1075 Bédard C, Kröger H, Destexhe A (2006) Does the 1/f frequency scaling of brain signals reflect self-organized critical
1076 states? *Phys Rev Lett* 97:118102 doi: 10.1103/PhysRevLett.97.118102.
- 1077 Beggs JM (2008) The criticality hypothesis: How local cortical networks might optimize information processing.
1078 *Philos Trans R Soc A Math Phys Eng Sci* 366:329–343 doi: 10.1098/rsta.2007.2092.
- 1079 Beggs JM, Plenz D (2003) Neuronal Avalanches in Neocortical Circuits. *J Neurosci* 23:11167–11177 doi:
1080 10.1523/JNEUROSCI.23-35-11167.2003.
- 1081 Beggs JM, Timme N (2012) Being critical of criticality in the brain. *Front Physiol* 3 JUN:163 doi:
1082 10.3389/fphys.2012.00163.

- 1083 Bender R, Lange S (2001) Adjusting for multiple testing - When and how? *J Clin Epidemiol* 54:343–349 doi:
1084 10.1016/S0895-4356(00)00314-0.
- 1085 Boerlin M, Machens CK, Denève S (2013) Predictive Coding of Dynamical Variables in Balanced Spiking Networks.
1086 *PLoS Comput Biol* 9:e1003258 doi: 10.1371/journal.pcbi.1003258.
- 1087 Bozdogan H (1987) Model selection and Akaike's Information Criterion (AIC): The general theory and its analytical
1088 extensions. *Psychometrika* 52:345–370 doi: 10.1007/BF02294361.
- 1089 Brunel N, Hakim V, Richardson MJE (2014) Single neuron dynamics and computation. *Curr Opin Neurobiol* 25:149–
1090 155 doi: 10.1016/j.conb.2014.01.005.
- 1091 Buzsáki G, Anastassiou CA, Koch C (2012) The origin of extracellular fields and currents-EEG, ECoG, LFP and spikes.
1092 *Nat Rev Neurosci* 13:407–420 doi: 10.1038/nrn3241.
- 1093 Carandini M, Ferster D (2000) Membrane potential and firing rate in cat primary visual cortex. *J Neurosci* 20:470–
1094 484 doi: 10.1098/rspb.1986.0060.
- 1095 Chialvo DR (2010) Emergent complex neural dynamics. *Nat Phys* 6:744–750 doi: 10.1038/nphys1803.
- 1096 Churchland MM et al. (2010) Stimulus onset quenches neural variability: a widespread cortical phenomenon. *Nat*
1097 *Neurosci* 13:369–378 doi: 10.1038/nn.2501.
- 1098 Clauset A, Shalizi CR, Newman MEJ (2009) Power-Law Distributions in Empirical Data. *SIAM Rev* 51:661–703 doi:
1099 10.1137/070710111.
- 1100 Clawson WP, Wright NC, Wessel R, Shew WL (2017) Adaptation towards scale-free dynamics improves cortical
1101 stimulus discrimination at the cost of reduced detection. *PLoS Comput Biol* 13:e1005574 doi:
1102 10.1371/journal.pcbi.1005574.
- 1103 Cocchi L, Gollo LL, Zalesky A, Breakspear M (2017) Criticality in the brain: A synthesis of neurobiology, models and
1104 cognition. *Prog Neurobiol* 158:132–152 doi: 10.1016/j.pneurobio.2017.07.002.
- 1105 Cowan JD, Neuman J, Kiewiet B, Van Drongelen W (2013) Self-organized criticality in a network of interacting

- 1106 neurons. *J Stat Mech Theory Exp* 2013:P04030 doi: 10.1088/1742-5468/2013/04/P04030.
- 1107 Crochet S, Poulet JFA, Kremer Y, Petersen CCH (2011) Synaptic mechanisms underlying sparse coding of active
1108 touch. *Neuron* 69:1160–1175 doi: 10.1016/j.neuron.2011.02.022.
- 1109 Crockett T, Wright N, Thornquist S, Ariel M, Wessel R (2015) Turtle dorsal cortex pyramidal neurons comprise two
1110 distinct cell types with indistinguishable visual responses. *PLoS One* 10:e0144012 doi:
1111 10.1371/journal.pone.0144012.
- 1112 Del Papa B, Priesemann V, Triesch J (2017) Criticality meets learning: Criticality signatures in a self-organizing
1113 recurrent neural network. *PLoS One* 12:e0178683 doi: 10.1371/journal.pone.0178683.
- 1114 Deluca A, Corral Á (2013) Fitting and goodness-of-fit test of non-truncated and truncated power-law distributions.
1115 *Acta Geophys* 61:1351–1394 doi: 10.2478/s11600-013-0154-9.
- 1116 Denève S, Machens CK (2016) Efficient codes and balanced networks. *Nat Neurosci* 19:375–382 doi:
1117 10.1038/nn.4243.
- 1118 Destexhe A, Paré D (1999) Impact of Network Activity on the Integrative Properties of Neocortical Pyramidal
1119 Neurons In Vivo. *J Neurophysiol* 81:1531–1547 doi: 10.1152/jn.1999.81.4.1531.
- 1120 Destexhe A, Rudolph M, Paré D (2003) The high-conductance state of neocortical neurons in vivo. *Nat Rev Neurosci*
1121 4:739–751 doi: 10.1038/nrn1198.
- 1122 Einevoll GT, Kayser C, Logothetis NK, Panzeri S (2013) Modelling and analysis of local field potentials for studying
1123 the function of cortical circuits. *Nat Rev Neurosci* 14:770–785 doi: 10.1038/nrn3599.
- 1124 El Boustani S, Marre O, Béhuret S, Baudot P, Yger P, Bal T, Destexhe A, Frégnac Y (2009) Network-state modulation
1125 of power-law frequency-scaling in visual cortical neurons. *PLoS Comput Biol* 5:e1000519 doi:
1126 10.1371/journal.pcbi.1000519.
- 1127 Fingelkurts AA, Fingelkurts AA, Neves CFH (2013) Consciousness as a phenomenon in the operational
1128 architectonics of brain organization: Criticality and self-organization considerations. *Chaos, Solitons &*

- 1129 Fractals 55:13–31 doi: 10.1016/j.chaos.2013.02.007.
- 1130 Freeman WJ, Cao TY (2008) Proposed Renormalization Group Analysis of Nonlinear Brain Dynamics at Criticality. In:
1131 Advances in cognitive neurodynamics : proceedings of the International Conference on Cognitive
1132 Neurodynamics, 2007 (Wang R, Shen E, Gu F, eds), pp 145–156. Springer. ISBN: 978-1-4020-8386-0.
- 1133 Friedman N, Ito S, Brinkman BAW, Shimono M, Deville REL, Dahmen KA, Beggs JM, Butler TC (2012) Universal
1134 critical dynamics in high resolution neuronal avalanche data. Phys Rev Lett 108:208102 doi:
1135 10.1103/PhysRevLett.108.208102.
- 1136 Friston K (2010) The free-energy principle: A unified brain theory? Nat Rev Neurosci 11:127–138 doi:
1137 10.1038/nrn2787.
- 1138 Gal A, Marom S (2013) Self-organized criticality in single-neuron excitability. Phys Rev E - Stat Nonlinear, Soft
1139 Matter Phys 88 doi: 10.1103/PhysRevE.88.062717.
- 1140 Gao L, Kostlan K, Wang Y, Wang X (2016) Distinct Subthreshold Mechanisms Underlying Rate-Coding Principles in
1141 Primate Auditory Cortex. Neuron 91:905–919 doi: 10.1016/j.neuron.2016.07.004.
- 1142 Gasparini S, Magee JC (2006) State-Dependent Dendritic Computation in Hippocampal CA1 Pyramidal Neurons. J
1143 Neurosci 26:2088–2100 doi: 10.1523/JNEUROSCI.4428-05.2006.
- 1144 Gatys LA, Ecker AS, Tchumatchenko T, Bethge M (2015) Synaptic unreliability facilitates information transmission in
1145 balanced cortical populations. Phys Rev E - Stat Nonlinear, Soft Matter Phys 91:62707 doi:
1146 10.1103/PhysRevE.91.062707.
- 1147 Gautam SH, Hoang TT, McClanahan K, Grady SK, Shew WL (2015) Maximizing Sensory Dynamic Range by Tuning
1148 the Cortical State to Criticality. PLoS Comput Biol 11:e1004576 doi: 10.1371/journal.pcbi.1004576.
- 1149 Gidas B (1989) A Renormalization Group Approach to Image Processing Problems. IEEE Trans Pattern Anal Mach
1150 Intell 11:164–180 doi: 10.1109/34.16712.
- 1151 Graupner M, Reyes AD (2013) Synaptic Input Correlations Leading to Membrane Potential Decorrelation of

- 1152 Spontaneous Activity in Cortex. *J Neurosci* 33:15075–15085 doi: 10.1523/JNEUROSCI.0347-13.2013.
- 1153 Hahn G, Petermann T, Havenith MN, Yu S, Singer W, Plenz D, Nikolic D (2010) Neuronal Avalanches in Spontaneous
1154 Activity In Vivo. *J Neurophysiol* 104:3312–3322 doi: 10.1152/jn.00953.2009.
- 1155 Haldeman C, Beggs JM (2005) Critical branching captures activity in living neural networks and maximizes the
1156 number of metastable states. *Phys Rev Lett* 94:58101 doi: 10.1103/PhysRevLett.94.058101.
- 1157 Hammond F, Malec JF, Nick T, Buschbacher RM (2015) Part II: Statistics, Introduction. In: *Handbook for Clinical*
1158 *Research: Design, Statistics, and Implementation*, pp 77–78. New York, NY: Demos Medical. ISBN: 978-1-
1159 936287-54-3.
- 1160 Hartley C, Taylor TJ, Kiss IZ, Farmer SF, Berthouze L (2014) Identification of criticality in neuronal avalanches: II. A
1161 theoretical and empirical investigation of the driven case. *J Math Neurosci* 4:1–42 doi: 10.1186/2190-8567-4-
1162 9.
- 1163 Heeger DJ (2017) Theory of cortical function. *Proc Natl Acad Sci USA* 114:1773–1782 doi:
1164 10.1073/pnas.1619788114.
- 1165 Hellwig B (2000) A quantitative analysis of the local connectivity between pyramidal neurons in layers 2/3 of the
1166 rat visual cortex. *Biol Cybern* 82:111–121 doi: 10.1007/PL00007964.
- 1167 Helmstaedter M (2013) Cellular-resolution connectomics: Challenges of dense neural circuit reconstruction. *Nat*
1168 *Methods* 10:501–507 doi: 10.1038/nmeth.2476.
- 1169 Hesse J, Gross T (2014) Self-organized criticality as a fundamental property of neural systems. *Front Syst Neurosci*
1170 8:166 doi: 10.3389/fnsys.2014.00166.
- 1171 Hulse BK, Lubenov E V., Siapas AG (2017) Brain State Dependence of Hippocampal Subthreshold Activity in Awake
1172 Mice. *Cell Rep* 18:136–147 doi: 10.1016/j.celrep.2016.11.084.
- 1173 Isaacson JS, Scanziani M (2011) How inhibition shapes cortical activity. *Neuron* 72:231–243 doi:
1174 10.1016/j.neuron.2011.09.027.

- 1175 Jeżewski W (2004) Scaling in weighted networks and complex systems. *Phys A Stat Mech its Appl* 337:336–356 doi:
1176 10.1016/j.physa.2004.01.028.
- 1177 Kajikawa Y, Schroeder CE (2011) How local is the local field potential? *Neuron* 72:847–858 doi:
1178 10.1016/j.neuron.2011.09.029.
- 1179 Karimipannah Y, Ma Z, Miller JK, Yuste R, Wessel R (2017a) Neocortical activity is stimulus- and scale-invariant. *PLoS*
1180 *One* 12:e0177396 doi: 10.1371/journal.pone.0177396.
- 1181 Karimipannah Y, Ma Z, Wessel R (2017b) Criticality predicts maximum irregularity in recurrent networks of
1182 excitatory nodes. *PLoS One* 12:e0182501 doi: 10.1371/journal.pone.0182501.
- 1183 Kello CT (2013) Critical branching neural networks. *Psychol Rev* 120:230–254 doi: 10.1037/a0030970.
- 1184 Kelly RC, Smith MA, Kass RE, Lee TS (2010) Local field potentials indicate network state and account for neuronal
1185 response variability. *J Comput Neurosci* 29:567–579 doi: 10.1007/s10827-009-0208-9.
- 1186 Kerby DS (2014) The Simple Difference Formula: An Approach to Teaching Nonparametric Correlation. *Compr*
1187 *Psychol* 3:11.IT.3.1 doi: 10.2466/11.IT.3.1.
- 1188 Kinouchi O, Copelli M (2006) Optimal dynamical range of excitable networks at criticality. *Nat Phys* 2:348–351 doi:
1189 10.1038/nphys289.
- 1190 Klaus A, Yu S, Plenz D (2011) Statistical analyses support power law distributions found in neuronal avalanches.
1191 *PLoS One* 6:e19779 doi: 10.1371/journal.pone.0019779.
- 1192 Koch-Janusz M, Ringel Z (2018) Mutual information, neural networks and the renormalization group. *Nat Phys*
1193 14:578–582 doi: 10.1038/s41567-018-0081-4.
- 1194 Kodandaramaiah SB, Franzesi GT, Chow BY, Boyden ES, Forest CR (2012) Automated whole-cell patch-clamp
1195 electrophysiology of neurons in vivo. *Nat Methods* 9:585–587 doi: 10.1038/nmeth.1993.
- 1196 Larkum ME, Watanabe S, Lasser-Ross N, Rhodes P, Ross WN (2008) Dendritic Properties of Turtle Pyramidal
1197 Neurons. *J Neurophysiol* 99:683–694 doi: 10.1152/jn.01076.2007.

- 1198 Larremore DB, Carpenter MY, Ott E, Restrepo JG (2012) Statistical properties of avalanches in networks. *Phys Rev E*
1199 - Stat Nonlinear, Soft Matter Phys 85:66131 doi: 10.1103/PhysRevE.85.066131.
- 1200 Larremore DB, Shew WL, Ott E, Restrepo JG (2011a) Effects of network topology, transmission delays, and
1201 refractoriness on the response of coupled excitable systems to a stochastic stimulus. *Chaos* 21:25117 doi:
1202 10.1063/1.3600760.
- 1203 Larremore DB, Shew WL, Ott E, Sorrentino F, Restrepo JG (2014) Inhibition causes ceaseless dynamics in networks
1204 of excitable nodes. *Phys Rev Lett* 112:138103 doi: 10.1103/PhysRevLett.112.138103.
- 1205 Larremore DB, Shew WL, Restrepo JG (2011b) Predicting criticality and dynamic range in complex networks: Effects
1206 of topology. *Phys Rev Lett* 106:58101 doi: 10.1103/PhysRevLett.106.058101.
- 1207 Laughlin RB (2014) Physics, Emergence, and the Connectome. *Neuron* 83:1253–1255 doi:
1208 10.1016/j.neuron.2014.08.006.
- 1209 Le Doussal P, Wiese KJ (2009) Size distributions of shocks and static avalanches from the functional
1210 renormalization group. *Phys Rev E - Stat Nonlinear, Soft Matter Phys* 79:51106 doi:
1211 10.1016/j.amjmed.2015.02.003.
- 1212 Lee AK, Brecht M (2018) Elucidating Neuronal Mechanisms Using Intracellular Recordings during Behavior. *Trends*
1213 *Neurosci* 41:385–403 doi: 10.1016/j.tins.2018.03.014.
- 1214 Lee WCA, Bonin V, Reed M, Graham BJ, Hood G, Glattfelder K, Reid RC (2016) Anatomy and function of an
1215 excitatory network in the visual cortex. *Nature* 532:370–374 doi: 10.1038/nature17192.
- 1216 Lee YC, Doolen G, Chen HH, Sun GZ, Maxwell T, Lee HY, Giles CL (1986) Machine Learning Using a Higher Order
1217 Correlation Network. *Phys D* 22:276–306 doi: 10.1016/0167-2789(86)90300-6.
- 1218 Levina A, Herrmann JM, Denker M (2007) Critical branching processes in neural networks. *Pamm* 7:1030701–
1219 1030702 doi: 10.1002/pamm.200700029.
- 1220 Levina A, Priesemann V (2017) Subsampling scaling. *Nat Commun* 8:15140 doi: 10.1038/ncomms15140.

- 1221 Litwin-Kumar A, Doiron B (2012) Slow dynamics and high variability in balanced cortical networks with clustered
1222 connections. *Nat Neurosci* 15:1498–1505 doi: 10.1038/nn.3220.
- 1223 Liu J, Newsome WT (2006) Local Field Potential in Cortical Area MT: Stimulus Tuning and Behavioral Correlations. *J*
1224 *Neurosci* 26:7779–7790 doi: 10.1523/JNEUROSCI.5052-05.2006.
- 1225 London M, Häusser M (2005) Dendritic Computation. *Annu Rev Neurosci* 28:503–532 doi:
1226 10.1146/annurev.neuro.28.061604.135703.
- 1227 Magee JC (2000) Dendritic integration of excitatory synaptic input. *Nat Rev Neurosci* 1:181–190 doi:
1228 10.1038/35044552.
- 1229 Malina KCK, Mohar B, Rappaport AN, Lampl I (2016) Local and thalamic origins of correlated ongoing and sensory-
1230 evoked cortical activities. *Nat Commun* 7:12740 doi: 10.1038/ncomms12740.
- 1231 Mao BQ, Hamzei-Sichani F, Aronov D, Froemke RC, Yuste R (2001) Dynamics of spontaneous activity in neocortical
1232 slices. *Neuron* 32:883–898 doi: 10.1016/S0896-6273(01)00518-9.
- 1233 Maris HJ, Kadanoff LP (1978) Teaching the renormalization group. *Am J Phys* 46:652–657 doi: 10.1119/1.11224.
- 1234 Marshall N, Timme NM, Bennett N, Ripp M, Lautzenhiser E, Beggs JM (2016) Analysis of Power Laws, Shape
1235 Collapses, and Neural Complexity: New Techniques and MATLAB Support via the NCC Toolbox. *Front Physiol*
1236 7:250 doi: 10.1109/EuCAP.2016.7481967.
- 1237 Mastrogiuseppe F, Ostojic S (2018) Linking Connectivity, Dynamics, and Computations in Low-Rank Recurrent
1238 Neural Networks. *Neuron* 99:609–623.e29 doi: 10.1016/j.neuron.2018.07.003.
- 1239 McGinley MJ, David S V., McCormick DA (2015) Cortical Membrane Potential Signature of Optimal States for
1240 Sensory Signal Detection. *Neuron* 87:179–192 doi: 10.1016/j.neuron.2015.05.038.
- 1241 Mehta P, Schwab DJ (2014) An exact mapping between the Variational Renormalization Group and Deep Learning.
1242 arXiv:14103831 doi: 10.1093/mnras/stv632.
- 1243 Meinecke DL, Peters A (1987) GABA immunoreactive neurons in rat visual cortex. *J Comp Neurol* 261:388–404 doi:

- 1244 10.1002/cne.902610305.
- 1245 Millman D, Mihalas S, Kirkwood A, Niebur E (2010) Self-organized criticality occurs in non-conservative neuronal
1246 networks during “up” states. *Nat Phys* 6:801–805 doi: 10.1038/nphys1757.
- 1247 Mokeichev A, Okun M, Barak O, Katz Y, Ben-Shahar O, Lampl I (2007) Stochastic Emergence of Repeating Cortical
1248 Motifs in Spontaneous Membrane Potential Fluctuations In Vivo. *Neuron* 53:413–425 doi:
1249 10.1016/j.neuron.2007.01.017.
- 1250 Moore JJ, Ravassard PM, Ho D, Acharya L, Kees AL, Vuong C, Mehta MR (2017) Dynamics of cortical dendritic
1251 membrane potential and spikes in freely behaving rats. *Science* (80-) 355:eaaj1497 doi:
1252 10.1126/science.aaj1497.
- 1253 Moretti P, Munoz MA (2013) Griffiths phases and the stretching of criticality in brain networks. *Nat Commun*
1254 4:2521 doi: 10.1038/ncomms3521.
- 1255 Mulligan KA, Ulinski PS (1990) Organization of geniculocortical projections in turtles: Isoazimuth lamellae in the
1256 visual cortex. *J Comp Neurol* 296:531–547 doi: 10.1002/cne.902960403.
- 1257 Ness T V., Remme MWH, Einevoll GT (2016) Active subthreshold dendritic conductances shape the local field
1258 potential. *J Physiol* 594:3809–3825 doi: 10.1113/JP272022.
- 1259 Nishimori H, Ortiz G (2011) *Elements of Phase Transitions and Critical Phenomena*. New York: Oxford University
1260 Press. doi: 10.1093/acprof:oso/9780199577224.001.0001.
- 1261 Nunez PL, Srinivasan R, Ingber L (2013) *Theoretical and Experimental Electrophysiology in Human Neocortex:
1262 Multiscale Dynamic Correlates of Conscious Experience*. In: *Multiscale Analysis and Nonlinear Dynamics*
1263 (Pesenson M (Meyer) Z, ed), pp 147–177. Weinheim, Germany: Wiley-VCH Verlag GmbH & Co. KGaA. ISBN:
1264 9783527671632.
- 1265 Okun M, Steinmetz NA, Cossell L, Iacaruso MF, Ko H, Barthó P, Moore T, Hofer SB, Mrsic-Flogel TD, Carandini M,
1266 Harris KD (2015) Diverse coupling of neurons to populations in sensory cortex. *Nature* 521:511–515 doi:
1267 10.1038/nature14273.

- 1268 Papanikolaou S, Bohn F, Sommer RL, Durin G, Zapperi S, Sethna JP (2011) Universality beyond power laws and the
1269 average avalanche shape. *Nat Phys* 7:316–320 doi: 10.1038/nphys1884.
- 1270 Perin R, Berger TK, Markram H (2011) A synaptic organizing principle for cortical neuronal groups. *Proc Natl Acad*
1271 *Sci* 108:5419–5424 doi: 10.1073/pnas.1016051108.
- 1272 Petersen CCH (2017) Whole-Cell Recording of Neuronal Membrane Potential during Behavior. *Neuron* 95:1266–
1273 1281 doi: 10.1016/j.neuron.2017.06.049.
- 1274 Pettersen KH, Lindén H, Tetzlaff T, Einevoll GT (2014) Power Laws from Linear Neuronal Cable Theory: Power
1275 Spectral Densities of the Soma Potential, Soma Membrane Current and Single-Neuron Contribution to the
1276 EEG. *PLoS Comput Biol* 10:e1003928 doi: 10.1371/journal.pcbi.1003928.
- 1277 Poil S-S, Hardstone R, Mansvelder HD, Linkenkaer-Hansen K (2012) Critical-State Dynamics of Avalanches and
1278 Oscillations Jointly Emerge from Balanced Excitation/Inhibition in Neuronal Networks. *J Neurosci* 32:9817–
1279 9823 doi: 10.1523/JNEUROSCI.5990-11.2012.
- 1280 Poil SS, Van Ooyen A, Linkenkaer-Hansen K (2008) Avalanche dynamics of human brain oscillations: Relation to
1281 critical branching processes and temporal correlations. *Hum Brain Mapp* 29:770–777 doi:
1282 10.1002/hbm.20590.
- 1283 Porta LD, Copelli M (2018) Modeling neuronal avalanches and long-range temporal correlations at the emergence
1284 of collective oscillations: continuously varying exponents mimic M/EEG results. *bioRxiv*:423921 doi:
1285 10.1101/423921.
- 1286 Poulet JFA, Petersen CCH (2008) Internal brain state regulates membrane potential synchrony in barrel cortex of
1287 behaving mice. *Nature* 454:881–885 doi: 10.1038/nature07150.
- 1288 Priesemann V (2014) Spike avalanches in vivo suggest a driven, slightly subcritical brain state. *Front Syst Neurosci*
1289 8:108 doi: 10.3389/fnsys.2014.00108.
- 1290 Priesemann V, Munk MHJ, Wibral M (2009) Subsampling effects in neuronal avalanche distributions recorded in
1291 vivo. *BMC Neurosci* 10:40 doi: 10.1186/1471-2202-10-40.

- 1292 Priesemann V, Shriki O (2018) Can a time varying external drive give rise to apparent criticality in neural systems?
1293 PLoS Comput Biol 14:e1006081 doi: 10.1371/journal.pcbi.1006081.
- 1294 Pruessner G (2012) Self-Organized Criticality Theory Models and Characterisation. Cambridge, UK ; New York:
1295 Cambridge University Press. ISBN: 9780521853354.
- 1296 Rapp PE, Albano AM, Zimmerman ID, Jiménez-Montaño MA (1994) Phase-randomized surrogates can produce
1297 spurious identifications of non-random structure. Phys Lett A 192:27–33 doi: 10.1016/0375-9601(94)91010-
1298 3.
- 1299 Ribeiro TL, Copelli M, Caixeta F, Belchior H, Chialvo DR, Nicolelis MAL, Ribeiro S (2010) Spike avalanches exhibit
1300 universal dynamics across the sleep-wake cycle. PLoS One 5:e14129 doi: 10.1371/journal.pone.0014129.
- 1301 Ribeiro TL, Ribeiro S, Belchior H, Caixeta F, Copelli M (2014) Undersampled critical branching processes on small-
1302 world and random networks fail to reproduce the statistics of spike avalanches. PLoS One 9:e94992 doi:
1303 10.1371/journal.pone.0094992.
- 1304 Roberts S (2018) Mathematician Carina Curto Thinks Like a Physicist to Solve Neuroscience Problems. Quanta Mag.
- 1305 Sachdev RNS, Ebner FF, Wilson CJ (2004) Effect of Subthreshold Up and Down States on the Whisker-Evoked
1306 Response in Somatosensory Cortex. J Neurophysiol 92:3511–3521 doi: 10.1152/jn.00347.2004.
- 1307 Sachidhanandam S, Sreenivasan V, Kyriakatos A, Kremer Y, Petersen CCH (2013) Membrane potential correlates of
1308 sensory perception in mouse barrel cortex. Nat Neurosci 16:1671–1677 doi: 10.1038/nn.3532.
- 1309 Saha D, Morton D, Ariel M, Wessel R (2011) Response properties of visual neurons in the turtle nucleus isthmi. J
1310 Comp Physiol A Neuroethol Sensory, Neural, Behav Physiol 197:153–165 doi: 10.1007/s00359-010-0596-3.
- 1311 Saremi S, Sejnowski TJ (2016) Correlated Percolation, Fractal Structures, and Scale-Invariant Distribution of Clusters
1312 in Natural Images. IEEE Trans Pattern Anal Mach Intell 38:1016–1020 doi: 10.1109/TPAMI.2015.2481402.
- 1313 Scarpetta S, Apicella I, Minati L, De Candia A (2018) Hysteresis, neural avalanches, and critical behavior near a first-
1314 order transition of a spiking neural network. Phys Rev E 97:62305 doi: 10.1103/PhysRevE.97.062305.

- 1315 Scarpetta S, Candia A de (2013) Neural Avalanches at the Critical Point between Replay and Non-Replay of
1316 Spatiotemporal Patterns. PLoS One 8:e64162 doi: 10.1371/journal.pone.0064162.
- 1317 Schwab DJ, Nemenman I, Mehta P (2014) Zipf's law and criticality in multivariate data without fine-tuning. Phys
1318 Rev Lett 113:68102 doi: 10.1103/PhysRevLett.113.068102.
- 1319 Senseman DM, Robbins KA (1999) Modal behavior of cortical neural networks during visual processing. J Neurosci
1320 19:RC3 (1-7) doi: 10.1523/JNEUROSCI.19-10-j0004.1999.
- 1321 Senseman DM, Robbins KA (2002) High-Speed VSD Imaging of Visually Evoked Cortical Waves: Decomposition Into
1322 Intra- and Intercortical Wave Motions. J Neurophysiol 87:1499–1514 doi: 10.1152/jn.00475.2001.
- 1323 Sethna JP, Dahmen KA, Myers CR (2001) Crackling noise. Nature 410:242–250 doi: 10.1038/35065675.
- 1324 Sfondrini A (2012) Introduction to universality and renormalization group techniques. Proc Sci 195 ISBN:
1325 9783540646662.
- 1326 Shaukat A, Thivierge J-P (2016) Statistical Evaluation of Waveform Collapse Reveals Scale-Free Properties of
1327 Neuronal Avalanches. Front Comput Neurosci 10:29 doi: 10.3389/fncom.2016.00029.
- 1328 Shew WL, Clawson WP, Pobst J, Karimipannah Y, Wright NC, Wessel R (2015) Adaptation to sensory input tunes
1329 visual cortex to criticality. Nat Phys 11:659–663 doi: 10.1038/nphys3370.
- 1330 Shew WL, Plenz D (2012) The Functional Benefits of Criticality in the Cortex. Neuroscientist 19:88–100 doi:
1331 10.1177/1073858412445487.
- 1332 Shew WL, Yang H, Yu S, Roy R, Plenz D (2011) Information Capacity and Transmission Are Maximized in Balanced
1333 Cortical Networks with Neuronal Avalanches. J Neurosci 31:55–63 doi: 10.1523/JNEUROSCI.4637-10.2011.
- 1334 Shimono M, Beggs JM (2015) Functional clusters, hubs, and communities in the cortical microconnectome. Cereb
1335 Cortex 25:3743–3757 doi: 10.1093/cercor/bhu252.
- 1336 Shoham S, O'Connor DH, Segev R (2006) How silent is the brain: Is there a “dark matter” problem in neuroscience?
1337 J Comp Physiol A Neuroethol Sensory, Neural, Behav Physiol 192:777–784 doi: 10.1007/s00359-006-0117-6.

- 1338 Shriki O, Alstott J, Carver F, Holroyd T, Henson RNA, Smith ML, Coppola R, Bullmore E, Plenz D (2013) Neuronal
1339 Avalanches in the Resting MEG of the Human Brain. *J Neurosci* 33:7079–7090 doi: 10.1523/JNEUROSCI.4286-
1340 12.2013.
- 1341 Shriki O, Yellin D (2016) Optimal Information Representation and Criticality in an Adaptive Sensory Recurrent
1342 Neuronal Network. *PLoS Comput Biol* 12:e1004698 doi: 10.1371/journal.pcbi.1004698.
- 1343 Song S, Reigl M, Nelson S, Chklovskii DB, Sjo PJ (2005) Highly Nonrandom Features of Synaptic Connectivity in Local
1344 Cortical Circuits. *PLoS Biol* 3 doi: 10.1371/journal.pbio.0030068.
- 1345 Stanley HE (1999) Scaling, universality, and renormalization: Three pillars of modern critical phenomena. *Rev Mod*
1346 *Phys* 71:S358–S366 doi: 10.1103/RevModPhys.71.S358.
- 1347 Stepanyants A, Hof PR, Chklovskii DB (2002) Geometry and structural plasticity of synaptic connectivity. *Neuron*
1348 34:275–288 doi: 10.1016/S0896-6273(02)00652-9.
- 1349 Stuart GJ, Spruston N (2015) Dendritic integration: 60 years of progress. *Nat Neurosci* 18:1713–1721 doi:
1350 10.1038/nn.4157.
- 1351 Taillefumier T, Magnasco MO (2013) A phase transition in the first passage of a Brownian process through a
1352 fluctuating boundary with implications for neural coding. *Proc Natl Acad Sci* 110:E1438–E1443 doi:
1353 10.1073/pnas.1212479110.
- 1354 Tang C, Bak P (1988) Critical exponents and scaling relations for self-organized critical phenomena. *Phys Rev Lett*
1355 60:2347–2350 doi: 10.1103/PhysRevLett.60.2347.
- 1356 Taylor TJ, Hartley C, Simon PL, Kiss IZ, Berthouze L (2013) Identification of criticality in neuronal avalanches: I. A
1357 theoretical investigation of the non-driven case. *J Math Neurosci* 3:1–26 doi: 10.1186/2190-8567-3-51-26.
- 1358 Theiler J, Eubank S, Longtin A, Galdrikian B, Doynne Farmer J (1992) Testing for nonlinearity in time series: the
1359 method of surrogate data. *Phys D Nonlinear Phenom* 58:77–94 doi: 10.1016/0167-2789(92)90102-S.
- 1360 Timme NM, Marshall NJ, Bennett N, Ripp M, Lautzenhiser E, Beggs JM (2016) Criticality maximizes complexity in

- 1361 neural tissue. *Front Physiol* 7:425 doi: 10.3389/fphys.2016.00425.
- 1362 Tishby N, Zaslavsky N (2015) Deep learning and the information bottleneck principle. In: 2015 IEEE Information
1363 Theory Workshop (ITW), pp 1–5. Jerusalem. doi: 10.1109/ITW.2015.7133169.
- 1364 Tomen N, Rotermund D, Ernst U (2014) Marginally subcritical dynamics explain enhanced stimulus discriminability
1365 under attention. *Front Syst Neurosci* 8:151 doi: 10.3389/fnsys.2014.00151.
- 1366 Touboul J, Destexhe A (2010) Can power-law scaling and neuronal avalanches arise from stochastic dynamics?
1367 *PLoS One* 5:e8982 doi: 10.1371/journal.pone.0008982.
- 1368 Touboul J, Destexhe A (2017) Power-law statistics and universal scaling in the absence of criticality. *Phys Rev E*
1369 95:12413 doi: 10.1103/PhysRevE.95.012413.
- 1370 Tsodyks M V., Markram H (1997) The neural code between neocortical pyramidal neurons depends on
1371 neurotransmitter release probability. *Proc Natl Acad Sci* 94:719–723 doi: 10.1073/pnas.94.2.719.
- 1372 Ulinski PS (1990) The Cerebral Cortex of Reptiles. In: *Comparative Structure and Evolution of Cerebral Cortex, Part I*
1373 (Jones EG, Peters A, eds), pp 139–215. New York: Plenum Press. doi: 10.1007/978-1-4757-9622-3_5.
- 1374 Werner G (2012) From brain states to mental phenomena via phase space transitions and renormalization group
1375 transformation: proposal of a theory. *Cogn Neurodyn* 6:199–202 doi: 10.1007/s11571-011-9187-4.
- 1376 Wertz A, Trenholm S, Yonehara K, Hillier D, Raics Z, Leinweber M, Szalay G, Ghanem A, Keller G, Rózsa B,
1377 Conzelmann KK, Roska B (2015) Single-cell-initiated monosynaptic tracing reveals layer-specific cortical
1378 network modules. *Science* (80-) 349:70–74 doi: 10.1126/science.aab1687.
- 1379 Willcox CR (1991) Understanding hierarchical neural network behaviour: a renormalization group approach. *J Phys*
1380 *A Math Theor* 24:2655 doi: 10.1088/0305-4470/24/11/030.
- 1381 Williams-García R V., Moore M, Beggs JM, Ortiz G (2014) Quasicritical brain dynamics on a nonequilibrium Widom
1382 line. *Phys Rev E - Stat Nonlinear, Soft Matter Phys* 90:62714 doi: 10.1103/PhysRevE.90.062714.
- 1383 Wilson DE, Whitney DE, Scholl B, Fitzpatrick D (2016) Orientation selectivity and the functional clustering of

- 1384 synaptic inputs in primary visual cortex. *Nat Neurosci* 19:1003–1009 doi: 10.1038/nn.4323.
- 1385 Wilting J, Priesemann V (2018) Inferring collective dynamical states from widely unobserved systems. *Nat Commun*
1386 9 doi: 10.1038/s41467-018-04725-4.
- 1387 Wolfe J, Houweling AR, Brecht M (2010) Sparse and powerful cortical spikes. *Curr Opin Neurobiol* 20:306–312 doi:
1388 10.1016/j.conb.2010.03.006.
- 1389 Wright NC, Hoseini MS, Wessel R (2017a) Adaptation modulates correlated subthreshold response variability in
1390 visual cortex. *J Neurophysiol* 118:1257–1269 doi: 10.1152/jn.00124.2017.
- 1391 Wright NC, Hoseini MS, Yasar TB, Wessel R (2017b) Coupling of synaptic inputs to local cortical activity differs
1392 among neurons and adapts after stimulus onset. *J Neurophysiol* 118:3345–3359 doi: 10.1152/jn.00398.2017.
- 1393 Wright NC, Wessel R (2017) Network activity influences the subthreshold and spiking visual responses of pyramidal
1394 neurons in the three-layer turtle cortex. *J Neurophysiol* 118:jn.00340.2017 doi: 10.1152/jn.00340.2017.
- 1395 Yaşar TB, Wright NC, Wessel R (2016) Inferring presynaptic population spiking from single-trial membrane
1396 potential recordings. *J Neurosci Methods* 259:13–21 doi: 10.1016/j.jneumeth.2015.11.019.
- 1397 Yu S, Klaus A, Yang H, Plenz D (2014) Scale-invariant neuronal avalanche dynamics and the cut-off in size
1398 distributions. *PLoS One* 9:e99761 doi: 10.1371/journal.pone.0099761.
- 1399
- 1400

1401

Figure Legends

1402

Figure 1: Will fluctuations in somatic membrane potential and comparable signals reflect the scale-free

1403

nature of neuronal avalanches from microelectrode array data? A recurrent network with excitatory (teal) and

1404

inhibitory (purple) neurons is measured in three ways: microelectrode array (MEA)(green/upper), whole-cell

1405

recording (red/middle), LFP (blue/bottom). Neuronal avalanches (highlighted in gold) are inferred from the

1406

population raster and fluctuations are analyzed like avalanches for the V_m and inverted LFP signals. Neuronal

1407

avalanches are defined as spurts of activity with quiet periods between them for MEA or excursions above the 25th

1408

percentile for continuous non-zero data. The ultimate question is whether membrane potential fluctuations will

1409

recapitulate the entire neuronal avalanche analysis previously conducted on MEA data, including power-laws in

1410

size and duration as well as a universal avalanche shape. This is abridged in the right most column which illustrates

1411

power-law distributions.

1412

Figure 2: Membrane potential fluctuations reveal signatures of critical point dynamics. Panel A shows

1413

the whole-brain eye attached joint V_m and LFP recording preparation. **Panel B** shows that the membrane potential

1414

(red) is thresholded at the 25th percentile (a dashed line). Avalanches are defined by excursions above this

1415

threshold. The gold region represents the size of the avalanche, which is the area between the signal and its 2nd

1416

percentile (a dashed line). The duration of the avalanche is the duration of the excursion. **Panel C** shows the size

1417

(left) and duration (right) distributions of V_m inferred avalanches when data is combined from seven recordings

1418

from the same neuron falling in the same 20-minute period. The comparison quotients (q) are both above 0.10

1419

(0.878 and 0.874 respectively), indicating that the size and duration distributions were better fits to power-laws at

1420

the given cut-off than 87% of power-laws produced by a random number generator with the same parameters

1421

(shown as a grey density cloud). N' indicates the number of avalanches above the lower cut-off of the fit (red

1422

vertical line) and N indicates the total number of avalanches. Size duration exponent denoted with τ while β is

1423

used for duration. **Panel D** shows the scaling relation which is a function relating average avalanche size to each

1424

given duration. The predicted exponent (γ_p) successfully explains 95.6% of the variance of a log-log

1425

representation of the data. A linear least squares regression could explain 96.7% and gives the fitted exponent

1426

(γ_f). Therefore, γ_p comes within 1.2% of the best linear explanation despite a 10% difference in exponent values.

1427 **Panel E** shows shape collapse. Each line represents the average time-course of an avalanches of a given duration.
 1428 The color indicates the duration according to the scale bar. Durations below 50 ms (the lower bound on turtle
 1429 pyramidal time-constants) are made translucent and slightly thickened. This shape collapse represents the global
 1430 collapse across all recordings in all cells. This confirms that a universal scaling function, $\mathcal{F}\left(\frac{t-t_0}{D}\right)$, is present. For
 1431 the seven recordings in the group represented in panels C & D, the mean scaling relation exponent derived from
 1432 shape collapse was $\gamma_{SC} = 1.23$ a disagreement of 2.2% relative to γ_f .

1433 **Figure 3: Membrane potential fluctuations are consistent with avalanches from previously obtained**
 1434 **microelectrode array data.** A plot of the exponents governing power-law scaling of avalanche duration vs the
 1435 exponents governing avalanche size. Circles indicate data which was best fit to a power-law in both its size and
 1436 duration. Triangle indicates otherwise (the MLE estimation of a would-be power-law fit, the “scaling index”, is
 1437 plotted in that case (Jeżewski, 2004)). Filled circles indicate data that meet all four standardized criteria for judging
 1438 data to be consistent with criticality. **Panel A** is a reproduction from (Shew et al., 2015). It shows the results of
 1439 avalanche analysis on microelectrode array data collected during the steady state of stimulus presentation in an
 1440 otherwise identical experimental preparation. The exponent values appear to covary to maintain a stable value of
 1441 the scaling relation $\gamma_p = \frac{\beta-1}{\tau-1}$. The correlation between β and τ was high (see Results: The Predicted Scaling
 1442 Relation Exponent is More Stable than Avalanche Size or Duration Exponents). **Panel B** shows the results of
 1443 avalanche analysis performed on fluctuations in subthreshold membrane potential. We found power-laws with
 1444 closely matching exponents and the same scaling relation with the similar level of stability. The correlation
 1445 between β and τ was high (see Results: The Predicted Scaling Relation Exponent is More Stable than Avalanche
 1446 Size or Duration Exponents).

1447 **Figure 4: The single-neuron estimate of network dynamics is optimized at the network critical point.**
 1448 **Panel A** illustrates model network consists of 10^4 excitatory (cyan) and inhibitory (magenta) model neurons with
 1449 sparse connectivity (line tips: arrows = excitation; circles = inhibition). The simulated model activity (raster plot) is
 1450 reresented in terms of the single-neuron spiking (raster plot) and the active fraction of the network $F(t) = S(t)/N$
 1451 where population spiking is $S(t)$. Concurrently, the smoothed inputs (orange) to a single neuron represents the

1452 V_m proxy, $\Phi_i(t)$. The threshold (dashed line) crossings of $\Phi_i(t)$ define avalanches (see Methods: Experimental
 1453 Design and Statistical Analysis). Avalanches of $F(t)$ and $\Phi_i(t)$ are analyzed in terms of their size (shown) and
 1454 duration (not shown) distributions and their corresponding exponents, τ . Avalanche statistics depend on several
 1455 network parameters including the critical branching tuning parameter λ . **Panel B** shows how the inclusion of
 1456 inhibition affects the network behavior. The black lines mark the boundaries of arbitrarily defined parameter
 1457 regions roughly corresponding to distinct kinds of behavior. The shade of blue indicates what fraction of ten trials
 1458 at each point met all four of our standardized criteria for consistency with expectations of critical branching
 1459 behavior. **Panel C** is a stacked area chart showing the probability density distribution of size exponent error
 1460 (between $F(t)$ and $\Phi_i(t)$) for different λ and dynamical regimes. The vertical thickness of each color band shows
 1461 the probability density for that subset of the data while the outer envelope shows the over-all probability density.
 1462 Probability density is estimated with a normal kernel smoothing function. In this panel we can see that power-law
 1463 scaling is most similar at criticality despite variability dependent on the parameter regime. **Panel D** shows a
 1464 complete summary of the tests for criticality when applied to $F(t)$ (top row) and $\Phi_i(t)$ (bottom row). From this we
 1465 can confirm that the system is consistent with criticality when there is no inhibition. The subsampling method
 1466 $\Phi_i(t)$ demonstrates consistency with criticality but displays a wider dispersion of exponent estimates. For
 1467 experimental V_m and MEA data there was a large correlation between β and τ showing that the scaling relation
 1468 (which predicts the slope of the trendline) is much more stable than exponent values. This is not the case for the
 1469 model where for $F(t)$ the correlation is low (see Results: The Predicted Scaling Relation Exponent is More Stable
 1470 than Avalanche Size or Duration Exponents).

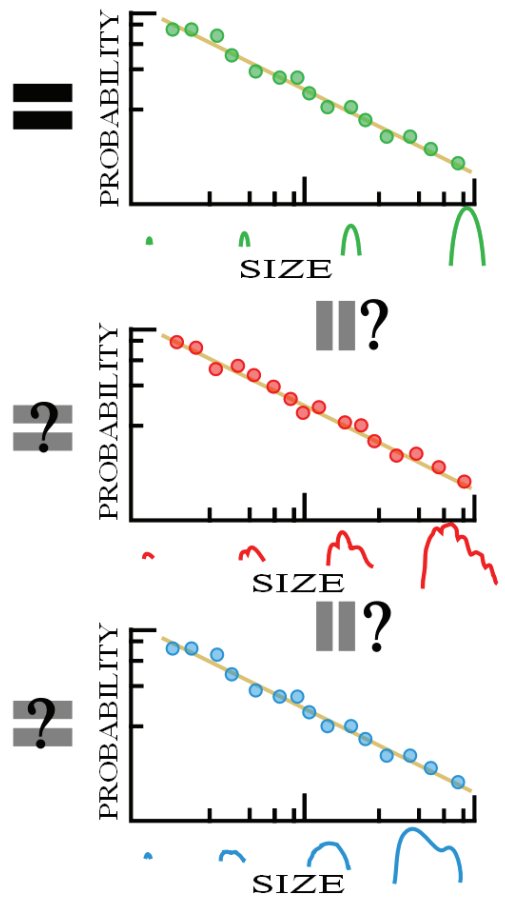
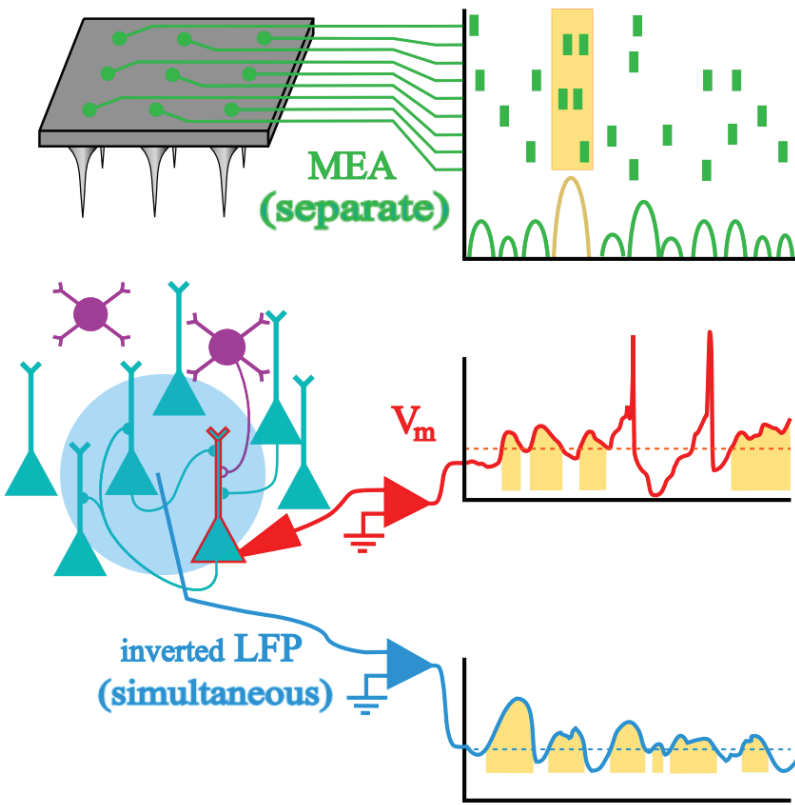
1471 **Figure 5: Inputs to a neuron stochastically estimate firing of its presynaptic pool in this critical branching**
 1472 **model.** **Panel A** shows differences in model activity dynamics with parameter regions (constant connectivity, $\lambda =$
 1473 1, but inhibition, χ varies). Each plot shows the active fraction of the network $F(t)$ in blue, the instantaneous firing
 1474 rate of node, $P_i(t)$, is in gold and the V_m proxy for the same node, $\Phi_i(t)$, is in orange. The node is randomly
 1475 selected from the nodes with degree within 10% of mean degree. The V_m proxy is produced by convolving the
 1476 firing rate of a single neuron with an alpha function with a 4 ms time constant. The top plot shows that with no
 1477 inhibition (or very little inhibition) activity in this parameter region dies away to zero and is unimodally distributed

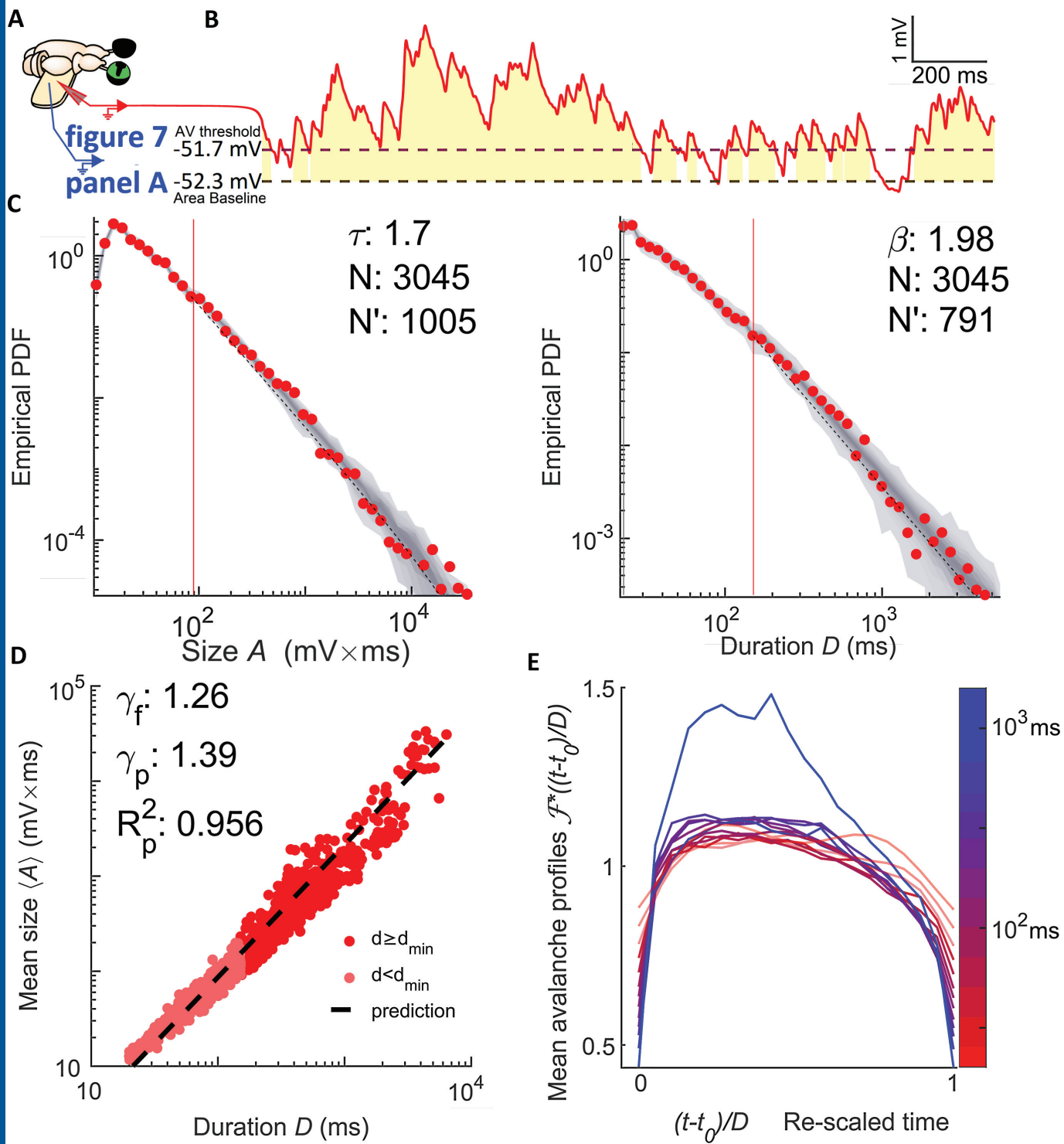
1478 about a small value. The middle plot shows that moderate amounts of inhibition results in self-sustained activity
 1479 that is bimodally distributed about one high and one low value. The bottom plot shows that when the fraction of
 1480 nodes that are inhibitory is much larger than connection density activity is self-sustaining and unimodally
 1481 distributed about a high value with low variance relative to the mean. **Panel B** shows the scaling relation for the
 1482 avalanches inferred from $\Phi_i(t)$ at different levels of inhibition, as in panel A. Inhibition detrimentally impacts the
 1483 validity of the scaling relation predictions, which are required for consistency with critical branching. The predicted
 1484 (γ_p) and fitted (γ_f) scaling exponents are indicated as is the goodness of fit (R_p^2) for the predicted exponent. **Panel**
 1485 **C** shows how avalanche (fluctuation) statistics vary with the parameter set displayed in panels A and B. The top
 1486 row shows avalanche (fluctuation) sizes, while the bottom row shows the duration distributions. Exponents τ (size
 1487 distribution) and β (duration distribution) as well as comparison quotients q are annotated on the plot. From these
 1488 plots, we can see that temporal smoothing ($\Phi_i(t)$) is necessary to accurately capture $F(t)$. Additionally, we see
 1489 that mismatch between the $F(t)$ and $P_i(t)$ avalanche distributions vary with network parameters. At high levels of
 1490 inhibition, the $i(t)$ avalanches are power-law distributed over smaller portions of their support. For $\Phi_i(t)$, neither
 1491 of the networks with less inhibition show the cut-offs associated with under sampling a critical branching network.

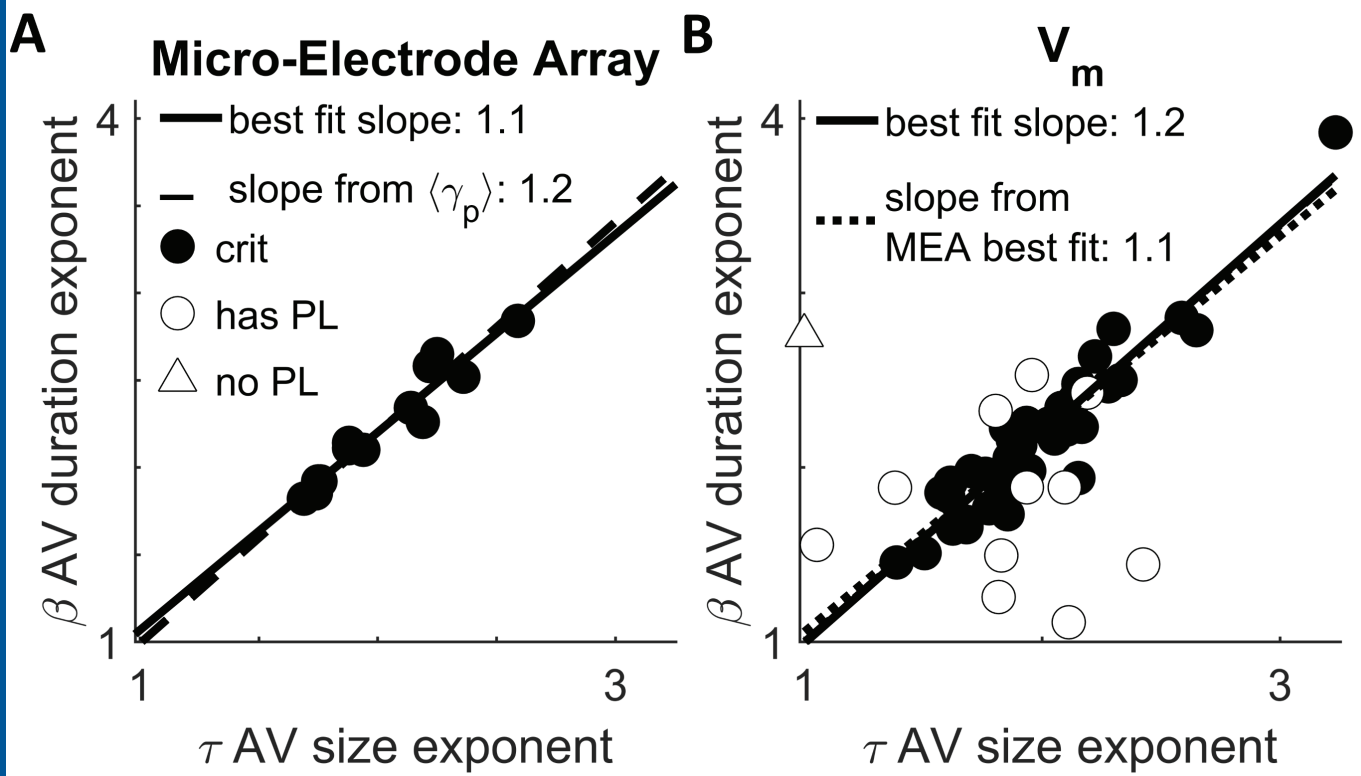
1492 **Figure 6: Comparison to surrogate signals reveals the importance of non-linearity and temporal**
 1493 **characteristics such as high-order correlation, proper combination of synaptic events, and signal time-scale.**
 1494 **Panel A** shows alternative signals and surrogate data time synchronized to figure 2B and showing thresholds and
 1495 integration baselines (dashed lines) with avalanche areas marked in yellow. The top row shows the inverted LFP
 1496 signal. The LFP is low-pass filtered (0-100 Hz), inverted, detrended and analyzed for avalanches identically to
 1497 membrane potentials. The second and third rows show the inferred excitatory inputs to a neuron. An algorithm
 1498 reconstructs the timing and shape of ePSPs from V_m . The resultant signal, g_{exc}^* , is much faster, making it analogous
 1499 to the $P_i(t)$ signal from the PIF model. This signal is smoothed (third row, see Methods: Model Simulations for
 1500 details) to produce a signal that is like V_m (Figure 2B) would be if it lacked IPSPs. The last row provides an example
 1501 of amplitude matched phase shuffled surrogate data (amplitude adjusted Fourier transform algorithm). **Panel B**
 1502 shows the scaling relation in the same order and dataset as panel A. The dashed line is the predicted scaling
 1503 relation exponent inferred from power-law fits to the size and duration distributions of positive fluctuations. In

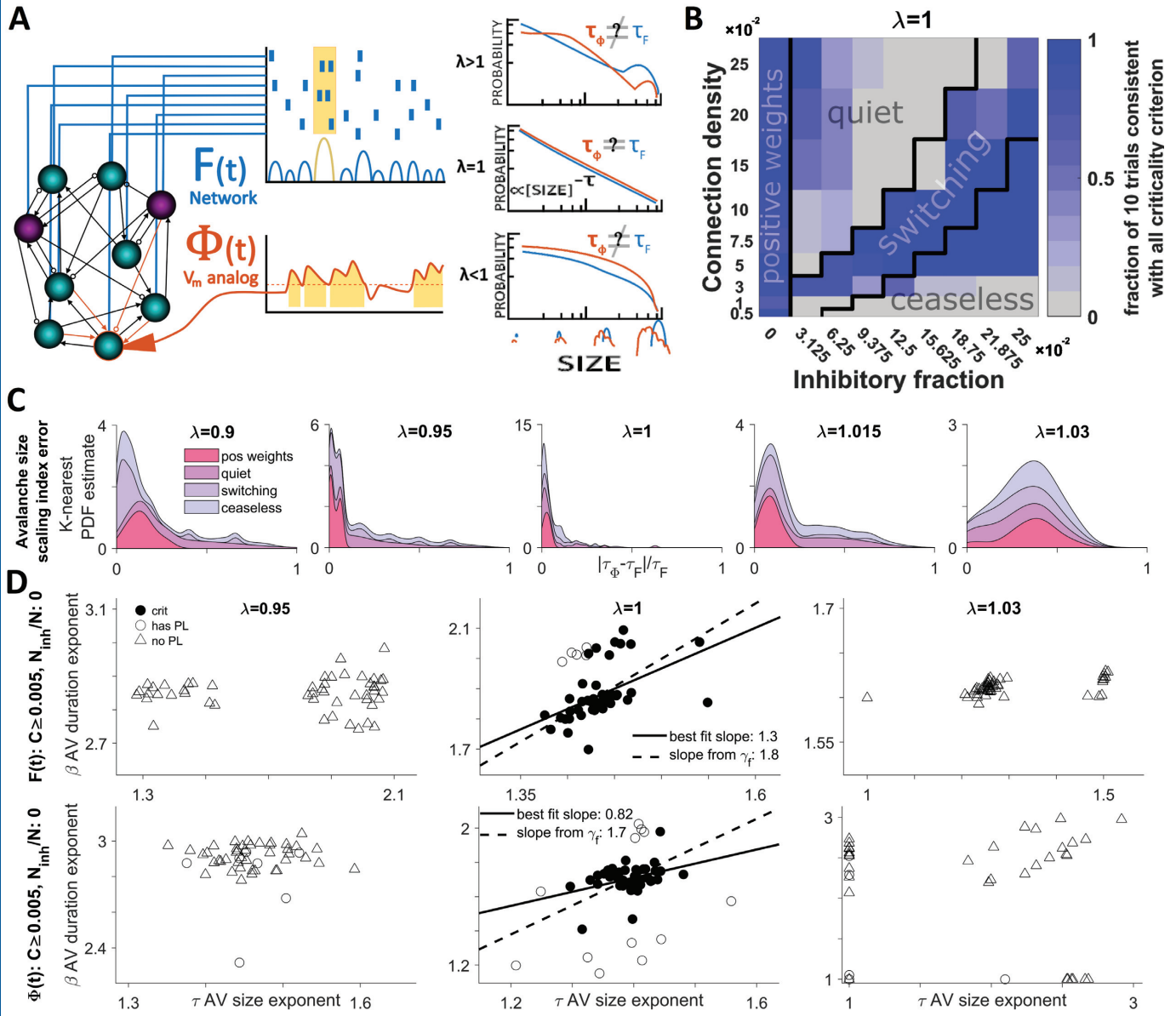
1504 cases where a power-law is not the best model the exponent nonetheless gives the average slope of a linear
 1505 regression on a log-log plot, a “scaling index” (Jeżewski, 2004). The predicted (γ_p) and fitted (γ_f) scaling exponents
 1506 are indicated as is the goodness of fit (R_p^2) for the predicted exponent. Mean size scales with duration for all signals
 1507 but often it is trivial ($\gamma_f \sim 1$) or poorly explained by a power-law ($R_f^2 < 0.95$), and it is rarely a good match with the
 1508 prediction from the scaling relation. **Panel C** shows shape collapse from the total dataset in the same order and
 1509 dataset as panel A. The color indicates the duration according to the scale bar. If self-similarity is present each
 1510 avalanche profile will collapse onto the same curve: $\mathcal{F}\left(\frac{t-t_0}{D}\right)$. The LFP illustrates a trivial scaling relation that is not
 1511 produced by true self-similarity: limited curvature and the exponents are very close to one. The second row shows
 1512 the reconstructed excitatory inputs, g_{exc}^* , and lacks shape collapse as expected from the lack of a scaling relation
 1513 power-law in panel B. The third row shows that sensible curvature re-emerges with smoothing but does not
 1514 produce a universal scaling function. In the last row the phase shuffled V_m shows a shape collapse which is worse
 1515 than for the original V_m (Figure 2E). **Panel D** shows size and duration distributions from each signal compared with
 1516 the V_m (in solid red). The phase shuffled V_m (dashed red) still obeys power-laws but the exponent values disagree,
 1517 and it less frequently meets our standardized criteria. Unsmoothed g_{exc}^* (solid gold) is more like inverted LFP than
 1518 anything else. When g_{exc}^* is smoothed (dashed gold) it becomes closer to the original V_m but retains pronounced
 1519 curvature in the duration distribution. We see V_m , AAFT, and smoothed g_{exc}^* produce distributions which extend
 1520 over similar orders of magnitude (~ 2). **Panel E** shows maximum value and curvature of the average profiles after
 1521 “collapse” as functions of duration. Shape collapse quality is a subjective measure, but these give a more
 1522 quantitative perspective. Good shape collapse should have a fixed maximum value and a high but fixed mean
 1523 curvature. For comparison, the UFT (Unwindowed or Unadjusted Fourier Transform) phase shuffled data is also
 1524 shown to provide a comparison to low curvature but a fixed maximum value. By visual inspection of AAFT and V_m it
 1525 is apparent that the asymmetry is gone and that deviation from the collapsed shape begins at shorter durations.
 1526 The max value diverges from a linear trend sooner for AAFT (~ 0.15 seconds, 0.5) than for V_m (~ 0.7 seconds).
 1527 Curvature also diverges sooner for the AAFT (0.5 seconds vs 0.7 seconds). Curvature does not become appreciable
 1528 until about 50-70 ms. Between the onset of curvature and divergence of max value there are $\log_{10}\left(\frac{0.15}{0.05}\right) \sim 0.48$
 1529 orders of magnitude for AAFT and $\log_{10}\left(\frac{0.7}{0.05}\right) \sim 1.15$ orders of magnitude for the original V_m .

1530 **Figure 7: Plausible alternative signals fail to demonstrate consistency with criticality.** A plot of the
1531 exponents governing power-law scaling of avalanche duration vs the exponents governing avalanche size. Circles
1532 indicate data which was best fit to a power-law in both its size and duration. Triangle indicates otherwise (the MLE
1533 estimation of a would-be power-law fit, the “scaling index”, is plotted in that case (Jeżewski, 2004)). Filled circles
1534 indicate data that meet all four standardized criteria for judging data to be consistent with criticality. We show the
1535 performance summary for the first group of data from each cell (the first 20-minute period which contained
1536 multiple recordings). The best fit slope is from linear regression to the plotted or indicated data, this is compared
1537 to the slope predicted by the mean γ_f (the exponent describing how avalanche size scales with duration). **Panel A**
1538 shows that positive fluctuations of inverted LFP were less likely to be power-law distributed and the power-law
1539 exponents tended to be unstable and not resemble MEA results. All 39 LFP datasets are represented. **Panel B**
1540 shows results from the reconstruction of excitatory input conductance g_{exc} . Only 12% were power-law distributed.
1541 The results do not resemble the MEA results. The slope from the trendline matches the scaling relation exponent
1542 but the regression is bad, $R^2 = 0.51$. **Panel C** shows how adding back some temporal smoothing to g_{exc}^* can
1543 improve results, 94% have power-laws but the exponents are more variable and generally larger. Most (96%) fail to
1544 have scaling relations which are well described by power-laws. The exponents β and τ are less independent but
1545 are not well described by the regression trendlines ($R^2 = 0.35$). The fit is applied only to the upper right cluster,
1546 excluding the outliers in the region $\beta < 1.6$ and $\tau < 1.6$. **Panel D** shows the summary of results from the AAFT
1547 phase shuffled V_m . As expected for a shuffling that preserves autocorrelation, power-laws are also preserved.
1548 However, the exponents are shifted down (especially the size distribution exponent). Far more fail to meet our
1549 criteria for consistency with criticality, as statistically significant difference (see Results: Stochastic Surrogates are
1550 Distinguishable from V_m or MEA Results, Reveals Importance of Non-Linear Filtering). Significantly fewer data sets
1551 have scaling relations well described by a power-law (75% as opposed to 90%), this is consistent with a slightly
1552 worse shape collapse (Figure 6C).

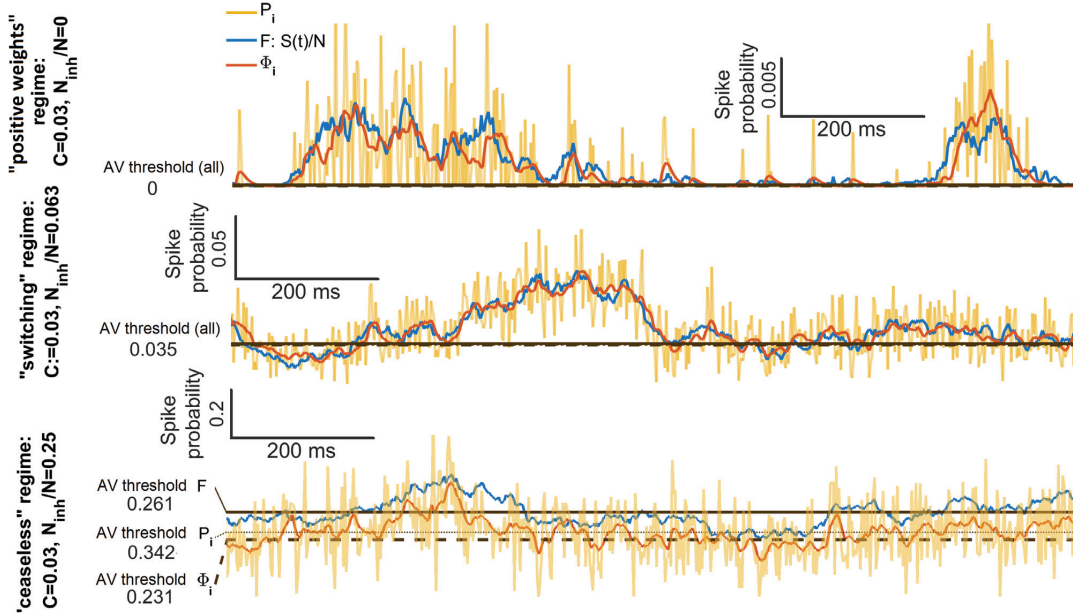




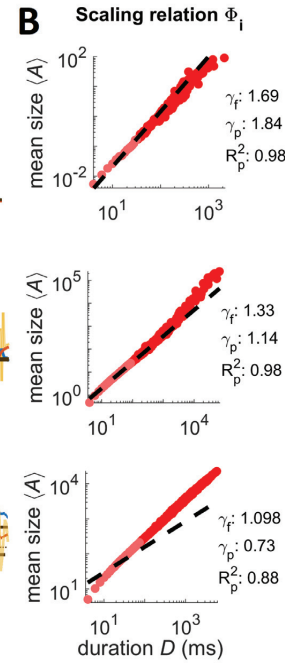




A



B



C

